

# Diffusion Creep of Sodic Amphibole-bearing Blueschist limited by Microboudinage

**Journal Article****Author(s):**

Tokle, Leif; Hufford, Lonnie J.; Behr, Whitney M.; Morales, Luiz F.G.; Madonna, Claudio

**Publication date:**

2023-09

**Permanent link:**

<https://doi.org/10.3929/ethz-b-000629257>

**Rights / license:**

[Creative Commons Attribution-NonCommercial 4.0 International](#)

**Originally published in:**




Journal of Geophysical Research: Solid Earth 128(9), <https://doi.org/10.1029/2023jb026848>

**Funding acknowledgement:**

947659 - Sediments and Subduction Interface Mechanics: from microscale creep to global plate tectonics (EC)



## Diffusion Creep of Sodic Amphibole-Bearing Blueschist Limited by Microboudinage

Leif Tokle<sup>1</sup> , Lonnie J. Hufford<sup>1</sup>, Whitney M. Behr<sup>1</sup> , Luiz F. G. Morales<sup>1,2</sup> , and Claudio Madonna<sup>1</sup> 

<sup>1</sup>Structural Geology and Tectonics Group, Department of Earth Sciences, Geological Institute, ETH Zürich, Zürich, Switzerland, <sup>2</sup>Scientific Center for Optical and Electron Microscopy (ScopeM), ETH Zürich, Zürich, Switzerland

### Key Points:

- Experimentally deformed sodic amphibole deforms by microboudinage with sodic-calcic amphibole diffusing into the boudin neck
- We developed a microboudinage flow law with a stress exponent of 2.0
- Extrapolation of the flow law provides viscosity estimates consistent with existing flow laws representative of the subduction interface

### Supporting Information:

Supporting Information may be found in the online version of this article.

### Correspondence to:

L. Tokle,  
Leif\_Tokle@alumni.brown.edu

### Citation:

Tokle, L., Hufford, L. J., Behr, W. M., Morales, L. F. G., & Madonna, C. (2023). Diffusion creep of sodic amphibole-bearing blueschist limited by microboudinage. *Journal of Geophysical Research: Solid Earth*, 128, e2023JB026848. <https://doi.org/10.1029/2023JB026848>

Received 3 APR 2023

Accepted 5 AUG 2023

### Author Contributions:

**Conceptualization:** Leif Tokle, Whitney M. Behr

**Data curation:** Leif Tokle

**Formal analysis:** Lonnie J. Hufford, Luiz F. G. Morales

**Investigation:** Leif Tokle

**Methodology:** Leif Tokle, Whitney M. Behr, Claudio Madonna

**Software:** Claudio Madonna

**Supervision:** Whitney M. Behr

**Visualization:** Leif Tokle, Whitney M. Behr

**Writing – original draft:** Leif Tokle

**Abstract** To investigate the mechanical and microstructural properties of mafic blueschists, we conducted deformation experiments on powdered natural blueschist aggregates using the general shear geometry in the Griggs apparatus. Experiments were performed at  $\sim 1.0$  GPa and temperatures ranging from 650 to 700°C. The blueschist starting material consists primarily of sodic amphibole and epidote, with minor amounts of quartz, titanite, albite, and white mica. Strain rate stepping experiments provided mechanical data with stress exponents ranging from 1.8 to 2.2. Microstructural analysis of the deformed samples show that the blueschist aggregates were deforming by microboudinage of the sodic amphibole, with a chemically new sodic-calcic amphibole diffused into the boudin neck. Based on these results, we interpret the samples to have deformed by diffusion creep of the sodic-calcic amphibole, which was rate-limited by diffusion into the boudin neck. We developed a microboudinage diffusion creep flow law using a least square regression, with parameters of  $A = 2.43e11 \text{ MPa}^{-n} \mu\text{m s}^{-1}$ ,  $n = 2.0 \pm 0.3$ ,  $m = 1.0$ , and  $Q = 384 \pm 15 \text{ kJ/mol}$ . Extrapolation of the flow law to the blueschist stability field suggests viscosities that are higher than metasedimentary rocks (quartz dislocation creep flow law) and lower than eclogitic rocks (omphacite dislocation creep flow law) consistent with field observations. We also show that this type of deformation mechanism matches observations of natural rocks in paleosubduction zone environments, supporting the application of this flow law to estimate amphibole rheology in modern subduction zones.

**Plain Language Summary** We conducted deformation experiments on samples of metamorphosed oceanic crust called blueschist, which is a rock abundant in sodium-rich amphibole and epidote. These rocks and minerals occur at high pressures ( $\sim 1$  GPa) and low temperatures ( $\sim 400^\circ\text{C}$ ) within the earth, primarily along the subduction zone interface. By conducting deformation experiments we can characterize and quantify the microstructural and mechanical properties of our samples. We find sodic amphibole, the most abundant mineral in our samples, deforms by a process called microboudinage, where the sodic amphibole fractures and new material simultaneously diffuses into the fracture, allowing the sample to accommodate strain. Using existing theory on microboudinage and the mechanical data from our deformation experiments, we develop a mechanical relationship (e.g., flow law) that can be extrapolated to geologic conditions to provide constraints on blueschist deformation along the subduction zone interface. To support the extrapolation of our flow law, we show that microboudinage has been widely observed in naturally deformed amphiboles from paleosubduction zone environments.

## 1. Introduction

Deformed mafic blueschists, which represent metamorphosed oceanic crust, are widespread in high pressure-low temperature terranes around the world, and are hallmarks of modern subduction (Ernst, 1973; Maruyama et al., 1996). Because mafic oceanic crustal rocks are commonly subducted, understanding the deformation mechanisms and rheological properties of blueschists is important for studying a range of subduction processes, such as interplate coupling (Agard et al., 2018; Conrad et al., 2004; Pacheco et al., 1993; Uyeda & Kanamori, 1979; Yañez & Cembrano, 2004), fluid and mass transfer (Bebout & Penniston-Dorland, 2016), interface seismic velocity structure (Abers, 2005; Hirose et al., 2008; Tewksbery-Christle et al., 2021), megathrust and intra-slab earthquakes (Incel et al., 2017; Muñoz-Montecinos, Angiboust, & Garcia-Casco, 2021; Muñoz-Montecinos, Angiboust, Garcia-Casco, Glodny, & Bebout, 2021; Okazaki & Hirth, 2016), slow slip and tremor processes (e.g., Audet & Kim, 2016; Audet & Schaeffer, 2018; Behr & Bürgmann, 2021; Fagerang & Sibson, 2010), and the overall strength of the subduction interface (Behr et al., 2022; Tulley et al., 2020).

© 2023 The Authors.

This is an open access article under the terms of the [Creative Commons Attribution-NonCommercial License](https://creativecommons.org/licenses/by-nc/4.0/), which permits use, distribution and reproduction in any medium, provided the original work is properly cited and is not used for commercial purposes.

**Writing – review & editing:** Leif Tokle, Lonnie J. Hufford, Whitney M. Behr, Luiz F. G. Morales, Claudio Madonna

One of the most abundant minerals in mafic blueschists is sodic amphibole, but its mechanical properties are not well understood. While some studies have focused on seismic anisotropy (Kim et al., 2013, 2015; Ko & Jung, 2015; Park & Jung, 2022; Park et al., 2020) and blueschist dehydration through eclogitization (Incel et al., 2017), few have explored the viscous flow properties of blueschist and sodic amphibole. Microanalytical and experimental work on amphiboles show a wide range of deformation mechanisms are possible from dislocation glide (Skrotzki, 1992), dislocation creep (Elyazadeh et al., 2018; Hacker & Christie, 1990; Reynard et al., 1989), diffusion creep (Getsinger & Hirth, 2014), cataclasis (Hacker & Christie, 1990; Muñoz-Montecinos et al., 2023; Nyman et al., 1992), semibrittle flow (Okazaki & Hirth, 2020), and reaction-driven creep (Condit & Mahan, 2018; Lee et al., 2022), but the conditions under which each mechanism should dominate in both nature and the laboratory are unknown.

Here we investigate the mechanical and microstructural properties of a powdered natural blueschist through deformation experiments using a Griggs apparatus. We demonstrate through combined mechanical and microstructural data that the blueschist deformed primarily by diffusion creep rate-limited by the process of microboudinage in amphibole, and we present a flow law that can be extrapolated to natural rocks that exhibit similar microphysical processes. We explore comparisons to natural blueschists and discuss implications for rheological properties of the subduction zone interface.

## 2. Methods

### 2.1. Starting Material

Samples were prepared by crushing a naturally foliated blueschist from the Condrey Mountain Window, CA, USA (Helper, 1986; Tewksbury-Christle et al., 2021). The starting material primarily contains sodic amphibole, epidote, titanite, and quartz with minor amounts of albite, white mica, and calcite. The crushed powder has a grain size range of ~30–150  $\mu\text{m}$ .

### 2.2. Experimental Procedures

Experiments were conducted in the Griggs apparatus in the Rock Physics and Mechanics Laboratory at ETH Zürich. All experiments were conducted in the general shear geometry, where grooved alumina shear pistons are cut at 45° to each other forming the shear geometry (Figure 1). Sample powder was placed between the two shear pistons and jacketed with a Pt sleeve where Ni foil was inserted between the alumina shear pistons and the Pt jacket. The assembly is weld-sealed using Pt cups at the ends of the shear pistons. All assemblies used a solid salt confining medium of NaCl with a K-type thermocouple. Three hydrostatic experiments were conducted at ~1.0 GPa, two at 700°C for 12 and 24 hr and one at 750°C for 48 hr. Five strain rate stepping experiments were conducted with three to five different strain rate steps where each deformation step reached a mechanical steady state. All strain rate stepping experiments were conducted at temperatures of 650, 675, and 700°C at 1.05  $\pm$  0.1 GPa confining pressure with shear strain rates from  $\sim 5 \times 10^{-7}$  to  $\sim 5 \times 10^{-5} \text{ s}^{-1}$ . One constant rate experiment was conducted at a shear strain rate of  $1.2 \times 10^{-5} \text{ s}^{-1}$  at 675°C and 1.0 GPa for comparison with the strain rate stepping experiment at 675°C. To preserve the microstructures, the temperature was lowered to 200°C at a rate of 4°C/s and then lowered to room pressure and temperature while maintaining a differential stress of a few hundred megapascals to suppress decompression cracking.

### 2.3. Post-Experiment Analysis Methods

After each experiment, samples were impregnated in epoxy and cut in half perpendicular to the shear plane and parallel to the shear direction. One half is used to make a thin section polished to a thickness of ~30  $\mu\text{m}$ . Cross-polarized light and scanning electron microscope (SEM) back-scattered electron (BSE) images were used to examine hydrostatic and deformation microstructures as well as mineral identification. Energy-dispersive X-ray spectroscopy (EDS) was also used for mineral identification. SEM-BSE images were used to measure the amphibole microboudin neck spacing for the deformation experiments and estimate mineral modal abundance. Electron backscatter diffraction (EBSD) was used to determine intragranular deformation and amphibole crystallographic preferred orientations (CPO). EBSD maps were acquired with a FEI/ThermoFisher Quanta 200 F SEM equipped with EDAX EBSD camera and TEAM software at ScopeM at ETH Zürich, using a 20 keV accelerating voltage, beam current of 8 nA, ~18 mm working distance, with maps ~200  $\mu\text{m} \times 200 \mu\text{m}$  in size with a step size of 100–200 nm. Post-processing data cleaning included standardization of confidence index (CI)

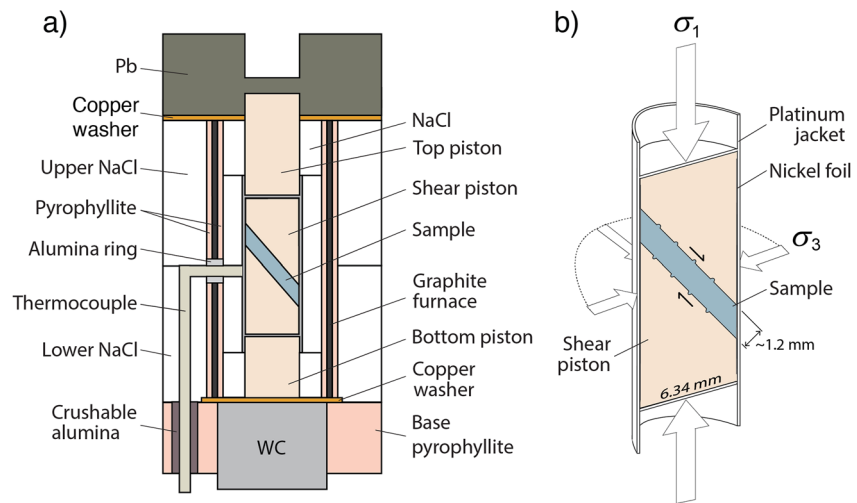


**Figure 1.** Illustration of the (a) solid salt assembly and (b) the cross-sectional view perpendicular to the shear plane of the jacketed sample prior to deformation. Modified from Holyoke and Kronenberg (2010) and Tokle, Hirth, and Stuntz (2023).

and neighbor CI correlation on OIM 8.5. Orientation distribution functions (ODFs) and plotting of pole figures were performed via the MTEX toolbox 5.8.1 for Matlab (Hielscher & Schaeben, 2008). ODFs were calculated assuming a halfwidth of  $10^\circ$  (bandwidth of 28 in spherical harmonic coefficients). For those calculations, only orientation data with  $CI > 0.1$  were considered. Pole figures are plotted using the experiment shear planes in the E-W position with a dextral shear sense. Quantitative major element data was collected for amphibole, epidote, titanite, and albite using the JEOL JXA-8230 electron probe microanalyzer (EPMA) at ETH Zürich (conditions and standards listed in Supporting Information S1).

## 2.4. Data Processing

The Griggs apparatus uses an external load cell to measure the force applied to the sample column. The displacement of the  $\sigma_1$  piston is measured using a linear variable differential transducer, where experimental data are recorded at a sampling rate of 1 Hz.  $\sigma_1$  piston displacement is corrected for apparatus compliance while the force is corrected for friction and sample thinning. Shear stresses and shear strain rates were converted to equivalent stress ( $\sigma_{\text{eqv}} = 2\tau$  where  $\tau$  is shear stress) and equivalent strain rate ( $\dot{\epsilon}_{\text{eqv}} = \frac{\dot{\gamma}}{\sqrt{3}}$ , where  $\dot{\gamma}$  is shear strain rate) following Paterson and Olgaard (2000). See Supporting Information S1 for the program information used to process the mechanical data. All experimental data are summarized in Table 1.

## 3. Results

### 3.1. Mechanical Data

All experiments achieved a mechanical steady state (Figure 2). The first deformation step in every deformation experiment shows strain weakening where a mechanical steady state is reached at a shear strain between 1.0 and 1.7. Strain weakening is not observed in any subsequent deformation steps except for the third deformation step in experiment LT036. All strain rate stepping experiments were deformed to a shear strain of  $\sim 2.2$  except LT036, which deformed to a shear strain of  $\sim 3.5$  (Figure 2). Plotting the steady state mechanical data in log stress versus log strain rate space, the five deformation experiments have stress exponents ranging between 1.8 and 2.2 (Figure 3a). The two  $675^\circ\text{C}$  experiments and the two  $650^\circ\text{C}$  strain rate stepping experiments show good mechanical reproducibility (Figures 2b, 2c, and 3).

### 3.2. Microstructures

#### 3.2.1. Hydrostatically Annealed Samples

Three hydrostatic experiments were conducted to characterize the microstructure prior to deformation. In the hydrostatically annealed samples, grains are randomly oriented and mineral phases are homogeneously distributed at the sample scale (Figure 4). Due to the high aspect ratio of the amphibole grains, there are regions locally



**Table 1**  
*Experimental Conditions and Mechanical Data*

Sample ID	Shear stress (MPa)	Equivalent stress (MPa)	Shear strain rate (s <sup>-1</sup> )	Equivalent strain rate (s <sup>-1</sup> )	Shear strain per step (total shear strain)	Temperature (°C)	Pressure (GPa)	Time at <i>P</i> and <i>T</i> prior to hit point (hr) <sup>a</sup>	Total time at <i>P</i> and <i>T</i> (hr) <sup>b</sup>	$\delta_{\text{Gln}}$ arithmetic mean ( $\mu\text{m}$ )	$\delta_{\text{Gln}}$ geometric mean ( $\mu\text{m}$ )	$\delta_{\text{Gln}}$ mode ( $\mu\text{m}$ )	$\delta_{\text{Gln}}$ standard deviation <sup>c</sup> ( $\mu\text{m}$ )
LT036a	165	330	4.6E-05	2.7E-05	1.06	700	1.06	21	88	-	-	-	-
b	41	82	3.8E-06	2.2E-06	0.29	-	1.07	-	-	-	-	-	-
c	146	292	4.5E-05	2.6E-05	1.47	-	1.07	-	-	-	-	-	-
d	75	150	1.3E-05	7.5E-06	0.65 (3.47)	-	1.07	-	-	2.2	1.9	1.6	1.3
LT048a	118	236	1.4E-05	7.8E-06	1.56	700	1.08	23	177	-	-	-	-
b	75	150	6.3E-06	3.6E-06	0.39	-	1.09	-	-	-	-	-	-
c	60	120	4.0E-06	2.3E-06	0.12	-	1.09	-	-	-	-	-	-
d	42	84	2.0E-06	1.2E-06	0.11 (2.18)	-	1.09	-	-	3.2	2.7	2.1	2.0
LT051a	163	326	1.4E-05	8.1E-06	1.32	675	1.06	19	100	-	-	-	-
b	104	208	6.5E-06	3.8E-06	0.39	-	1.06	-	-	-	-	-	-
c	62	124	2.4E-06	1.4E-06	0.25 (1.96)	-	1.06	-	-	2.0	1.7	1.4	1.0
LT044a	185	370	5.1E-06	2.9E-06	0.97	650	1.06	45	338	-	-	-	-
b	251	502	1.3E-05	7.5E-06	0.54	-	1.07	-	-	-	-	-	-
c	139	278	2.2E-06	1.3E-06	0.42	-	1.07	-	-	-	-	-	-
d	78	156	9.0E-07	5.2E-07	0.24 (2.17)	-	1.07	-	-	2.1	1.9	1.6	1.1
LT066a	180	360	4.0E-06	2.3E-06	1.46	650	1.04	48	372	-	-	-	-
b	140	280	2.6E-06	1.5E-06	0.25	-	1.05	-	-	-	-	-	-
c	98	196	1.3E-06	7.5E-07	0.39	-	1.05	-	-	-	-	-	-
d	75	150	8.5E-07	4.9E-07	0.17 (2.27)	-	1.05	-	-	2.1	1.8	1.3	1.1
LT073	175	350	1.3E-05	7.5E-06	(1.3)	675	1.05	22	62	2.1	1.9	2.0	1.9
LT047	-	-	-	-	-	700	1.02	12	12	-	-	-	-
LT057	-	-	-	-	-	700	1.04	24	24	-	-	-	-
LT056	-	-	-	-	-	750	1.02	48	48	-	-	-	-

<sup>a</sup>Time at *P* and *T* prior to the hit point refers to the time when deformation conditions were reached during pressurization to the hit point. <sup>b</sup>Total time at *P* and *T* refers to the total amount of time each experiment was at the maximum pressure and temperature conditions to the nearest hour. <sup>c</sup>Standard deviation represents 1 $\sigma$  uncertainty.

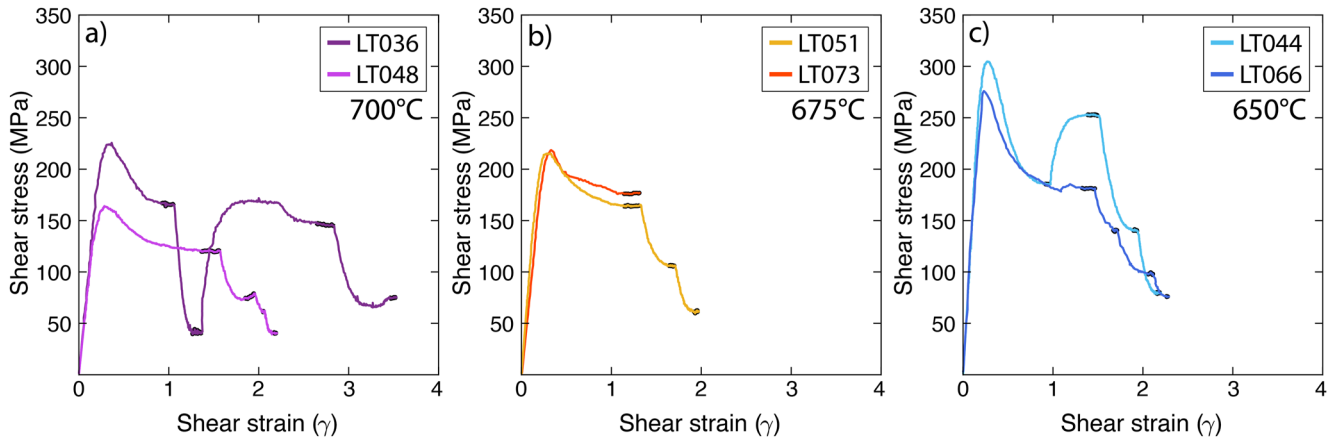


**Figure 2.** Plots of shear strain versus shear stress for the constant rate and strain rate stepping experiments. Regions highlighted in black represent the mechanical steady state.

where amphibole grains align (see bottom right region of Figure 4b); however, the local alignment is random relative to the  $\sigma_1$  orientation (Figure 4b). Grain crushing is observed in all mineral phases as a result of pressurizing and compacting the starting powder. Microboudinage is not observed in the hydrostatic samples (Figure 4). Hydrostatic sample LT047 has a relatively strong initial crystallographic preferred orientation (CPO), with (100) maxima subparallel to the pole of the shear plane, a weak girdle of (001) poles distributed along the shear plane and a more uniform distribution of the poles to (010) interpreted to occur due to rigid body rotation during pressurization (Figure 4c). The two 700°C hydrostatic samples show a metamorphic reaction of the starting mineral assemblage, notable by chemical zonation within the amphibole and the crystallization of albite, where the reaction is further progressed in the 24-hr sample (Figure 4; see Section 3.3). Albite grains that crystallize as part of the metamorphic reaction are a few microns in size while albite that originates from the starting powder have grain sizes  $>20 \mu\text{m}$  (Figure 4). EBSD analyses of the hydrostatic samples show indexing of albite, indicating it is not amorphous at deformation conditions (Figure S1 in Supporting Information S1). Microstructures from a 48-hr hydrostatic sample conducted at 750°C and 1.0 GPa shows nearly all of the sodic amphibole and titanite have been replaced by sodic-calcic amphibole and ilmenite (Figure S1 in Supporting Information S1; see Section 3.3). Based on the change in microstructures and mineral assemblage in the 750°C sample, the maximum temperature of our deformation experiments is limited to 700°C. Estimated mineral abundance for the hydrostatic samples are plotted in Figure 4d.

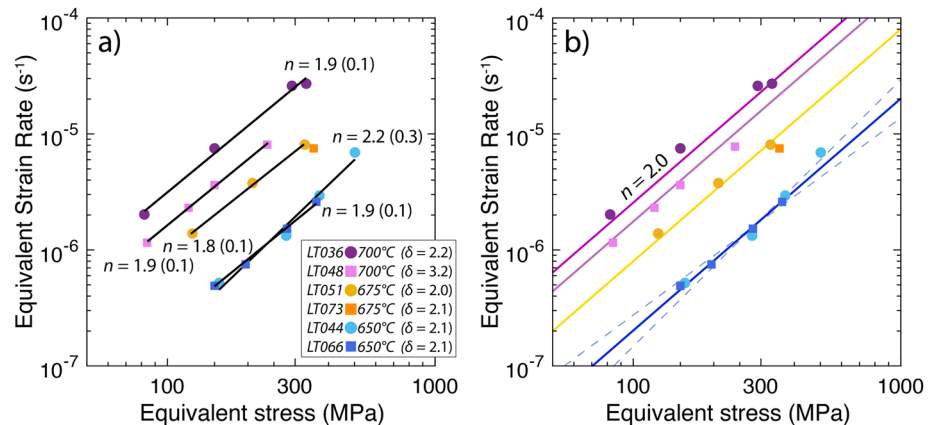


**Figure 3.** Plots of equivalent stress versus equivalent strain rate (a) showing the stress exponent fits for each strain rate stepping experiment and (b) a comparison between the flow law and the mechanical data. In (a),  $\delta$  represents the average microboudin neck length in microns calculated using the arithmetic mean. (a) Stress exponent values and  $1\sigma$  uncertainty are calculated using the Matlab function *robustfit*, where (0.1) is “ $\pm 0.1$ .” The dashed lines in (b) represent the uncertainty in the flow law based on the uncertainty in  $n$  ( $2.0 \pm 0.3$ ).

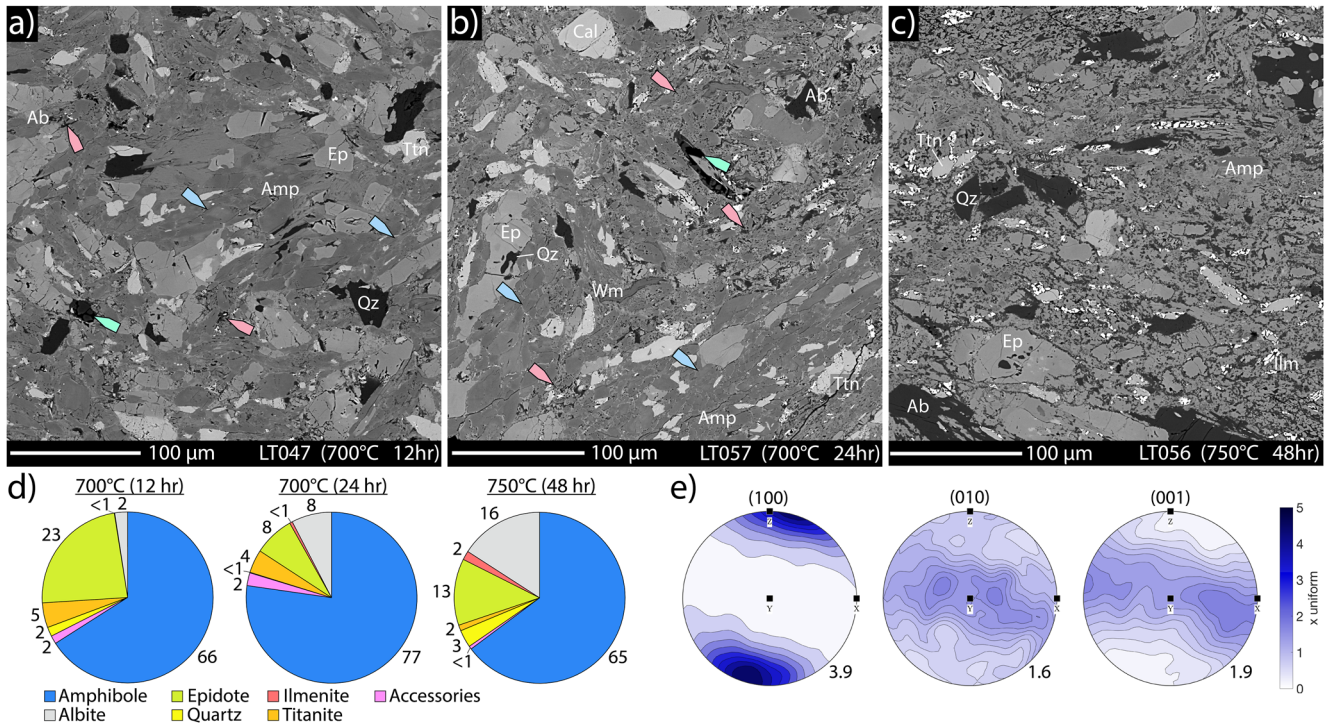


**Figure 4.** SEM-BSE photomicrographs of hydrostatic experiments that were annealed for (a) 12 hr and (b) 24 hr at 700°C and (c) 48 hr at 750°C at 1 GPa. Blue arrows show chemical zonation in amphibole, red arrows show regions of albite as a reaction product, and green arrows show the similar greyscale color between quartz and albite in the back-scattered electron (BSE) photomicrographs. (d) Pie charts showing the estimated phase abundance calculated from the BSE images in (a–c). Due to their low abundance white micas and calcite are listed as Accessory phases. (e) Amphibole pole figures of hydrostatic experiment LT047 with maxima displayed to the bottom right of each pole figure (multiples of uniform distribution—MUD). The phase map of the region used to calculate the amphibole CPO is shown in Figure S1 of the Supporting Information S1. The shear plane is parallel to the horizontal plane of each photomicrograph. Amp—amphibole, Qz—quartz, Ab—albite, Ep—Epidote, Ttn—titanite, Ilm—ilmenite, Cal—calcite, Wm—white mica.

### 3.2.2. Deformed Samples

All deformed samples develop an S-C-C' foliation at the sample scale with amphibole and titanite defining the S- and C-planes (Figures 5 and 6). The foliation varies in orientation from sub-parallel to the shear plane to ~25° antithetic to the shear direction, where antithetic refers to rotations opposite the shearing direction with the shear plane

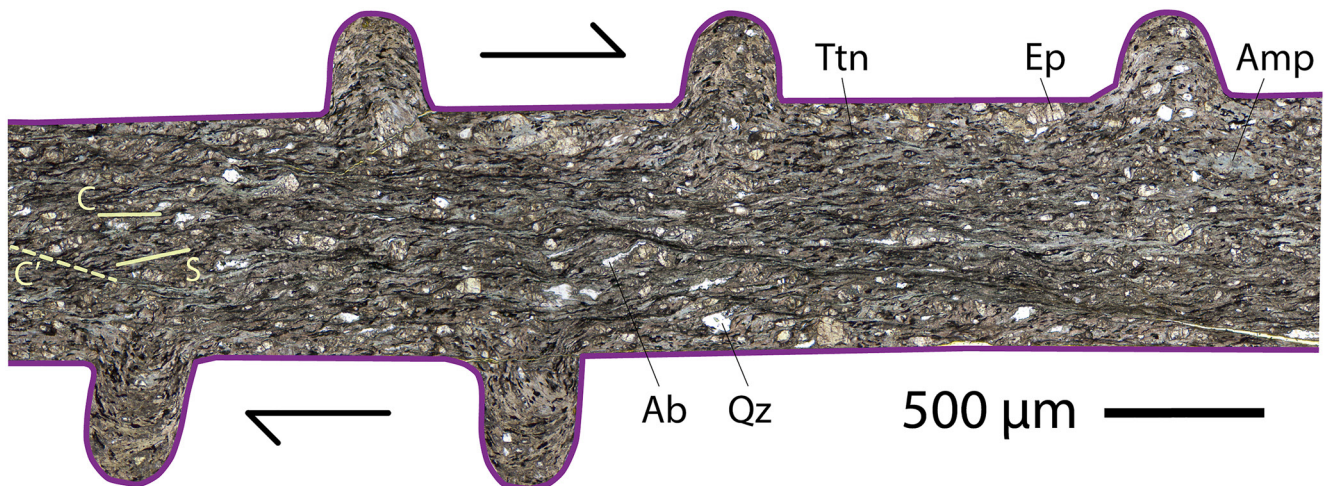


**Figure 5.** Plane polarized light photomicrograph of the central portion of deformed sample LT036 (700°C) where the purple line outlines the sample-piston interface. The yellow color filling the crack in the bottom right is epoxy used for thin section preparation. Amp—amphibole, Qz—quartz, Ab—albite, Ep—Epidote, Ttn—titanite.



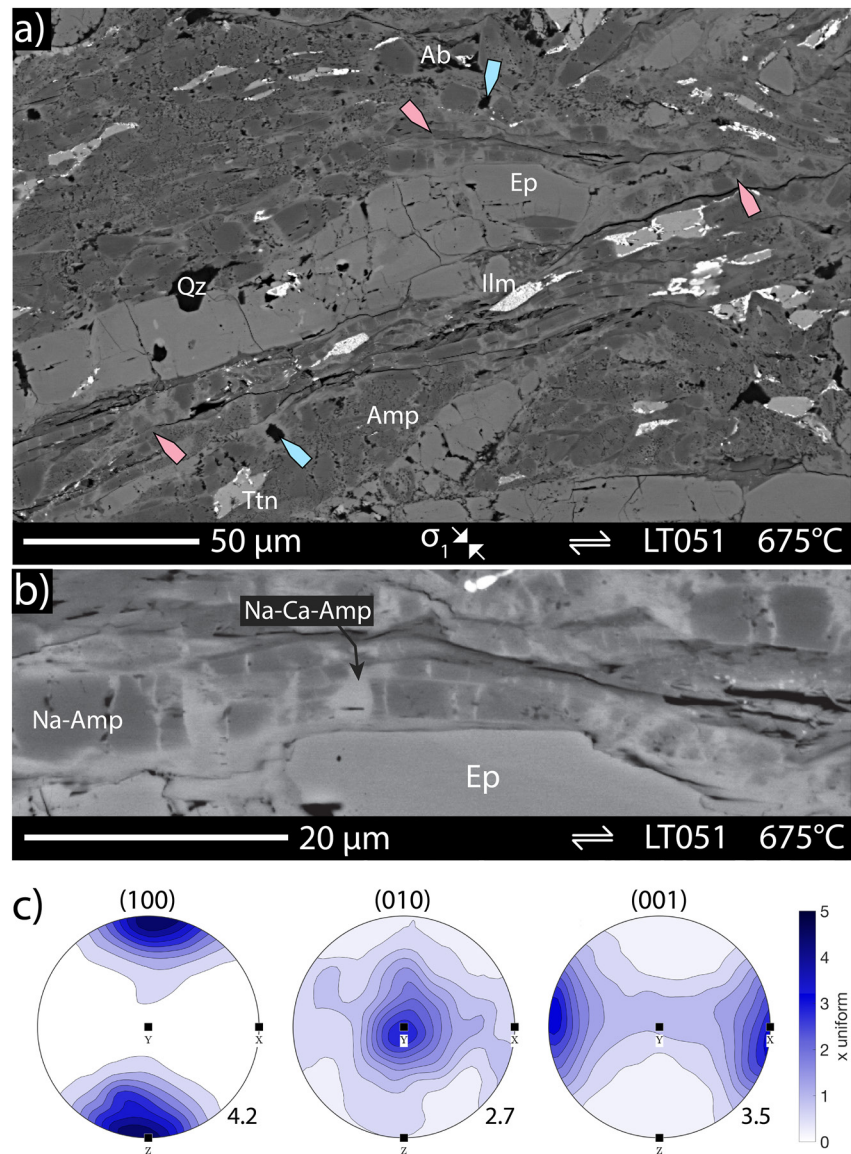


**Figure 6.** SEM-BSE photomicrographs showing deformation microstructures and representative amphibole pole figures. (a) Red arrows show examples of amphibole microboudinage and blue arrows show examples of albite in the microboudin necks. (b) Close-up photomicrograph of amphibole microboudinage from the central region in (a) just above the “Ep” label. (c) Amphibole pole figures for deformed sample LT048 (700°C), with maxima displayed to the bottom right of each pole figure (multiples of uniform distribution—MUD). The shear plane is parallel to the horizontal plane of each photomicrograph with a dextral shear sense for both the photomicrographs and CPO. Amp—amphibole, Qz—quartz, Ab—albite, Ep—Epidote, Ttn—titanite, Ilm—ilmenite.

representing 0° (Figures 5 and 6). Variation in the foliation is due to amphibole grains wrapping around rigid epidote and quartz grains (Figures 5 and 6). C'-shear bands develop in all samples at ~30° synthetic to the shear direction and range from one hundred to several hundred microns in length and in some cases extend through most of the sample (Figures 5 and 7). C'-shear bands are defined by localized deformation of sodic-calcic amphibole, albite, ilmenite, and small rigidly rotating sodic amphibole grains (Figure 7). Shear offset in minerals such as epidote, albite, and amphibole show the C'-shear bands have a shear sense consistent with the experiments shearing direction (Figure 7).

Deformation at the sample scale is ductile, however, there is a range of deformation microstructures observed within the different minerals. Epidote, titanite, and quartz do not accommodate plastic strain (Figures 5–7). Epidote shows fractures that commonly span the length of the grains and are filled with either quartz or albite (Figures 5, 6a, and 7; Figure S2 in Supporting Information S1). Fracturing in epidote also leads to moderate grain

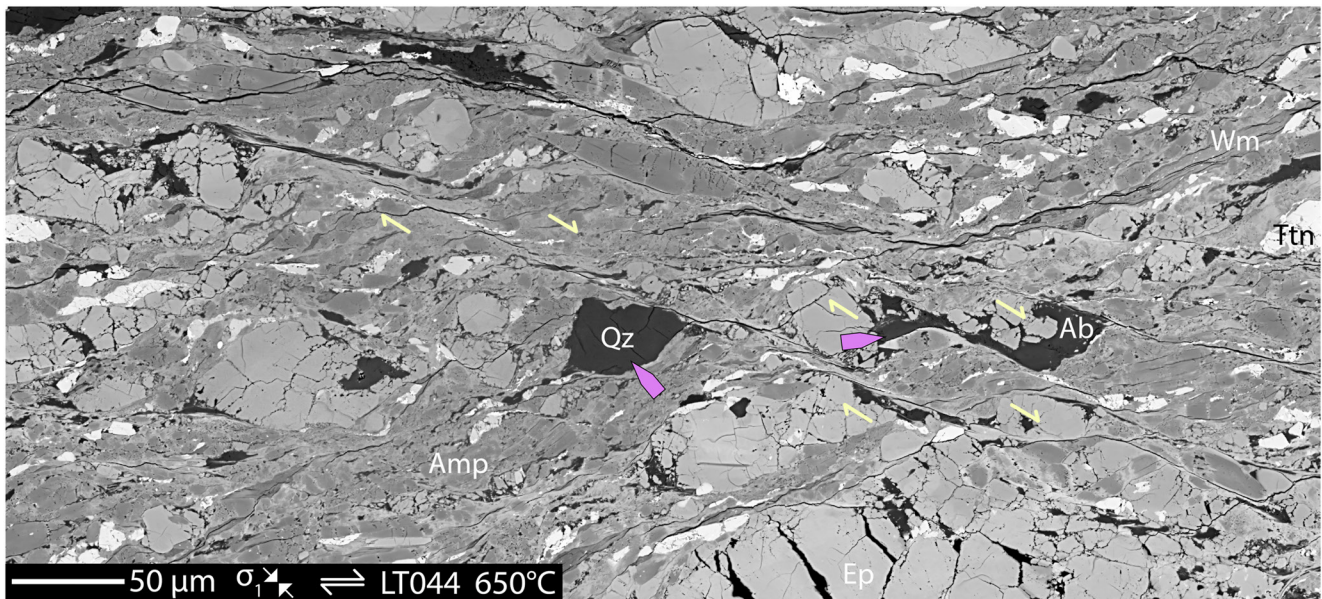


**Figure 7.** SEM-BSE photomicrograph highlighting  $C'$ -shear bands. Yellow arrows outline the orientation and shear direction for several  $C'$ -shear bands. Purple arrows highlight the different amount of strain accumulation between quartz and albite even though they look similar in BSE. Brightness and contrast were modified to emphasize amphibole microstructures, as a result titanite and ilmenite are both white and difficult to distinguish. The shear plane is parallel to the horizontal plane of the photomicrograph with a dextral shear sense. Amp—amphibole, Qz—quartz, Ab—albite, Ep—Epidote, Ttn—titanite, Wm—white mica.

size reduction in some places (Figures 5 and 7). Amphibole, albite, and ilmenite accommodate plastic strain within the samples with amphibole accommodating the majority of the strain due to its greater abundance. Albite and ilmenite grains are isolated and do not form interconnected layers (Figures 6–8). Albite is commonly found in strain shadows of large epidote and quartz grains as well as in  $C'$ -shear bands. Large albite grains are distinguishable from quartz in BSE photomicrographs as they accommodate a significant amount of strain relative to quartz (purple arrows in Figure 7).

Amphibole grains show microboudinage where the original sodic amphibole fractures, primarily along the (001) plane, and a compositionally new sodic-calcic amphibole fills the fracture forming a microboudin neck. The majority of fractures involving microboudinage cut across the whole grain (Figures 6–8). Many microboudin necks contain both sodic-calcic amphibole and albite, with either a mixed/intergrowth texture (blue arrows in Figure 8a) or an unmixed texture (blue arrows in Figure 6a). Microboudin necks range in length from  $\sim 0.5$  to  $\sim 10$   $\mu\text{m}$ . Microboudinage in amphibole is more abundant in the high strain sample (LT036,  $\gamma = 3.47$ ) in comparison to the lower strain samples ( $\gamma \sim 2.2$ ) (Figure S3 in Supporting Information S1). In all samples there are regions where microboudinage is heterogeneous, where some amphibole grains show a significant amount of microboudins (e.g., high strain regions) next to grains with little to no microboudins (e.g., low strain regions), regardless of grain orientation (Figure 6a). There are also regions in all samples that exhibit homogenous microboudinage, where the amount of microboudins (e.g., strain) is more uniform (Figure 7). There is no systematic relationship between the spacing of microboudins within a sodic amphibole grain, and no obvious correlation between the initial grain size of sodic amphibole and microboudin neck length (Figure 6). Grains with higher aspect ratios typically have more microboudins than grains with lower aspect ratios (Figures 6 and 7).

Correlation between a BSE photomicrograph and a grain reference orientation deviation (GROD) angle map from the same region shows microboudinage causes sharp changes in crystal orientation relative to the grain average orientation. This change in grain orientation results in low and high angle grain boundaries at microboudin necks (Figure 8). The GROD map also shows most sodic amphibole grains have little to no internal deformation away from microboudin necks, however, there are a few sodic amphibole grains that show gradational changes in misorientation that do not correlate with microboudinage (star in Figure 8). The CPO of the deformed amphibole in sample LT051 shows strong maxima (Figure 6c). In comparison to the hydrostatic amphibole CPO, the deformed amphibole shows a stronger (010) and (001) maximum (Figures 4e and 6c). Note that the calculated CPO of the deformed samples is a bulk measurement of both the sodic and sodic-calcic amphiboles.



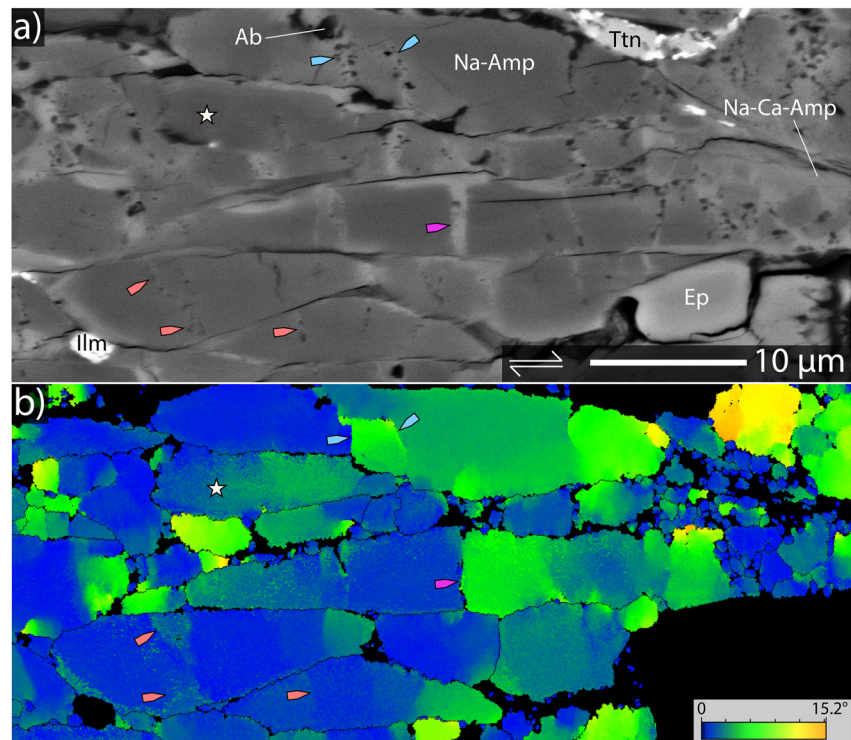
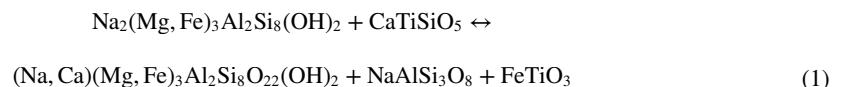


**Figure 8.** SEM-derived images of microboudinage in amphibole from (a) BSE photomicrograph and (b) internal strain based on a grain reference orientation deviation map of the same area. (b) Non-indexed regions and/or phases that are not amphibole are shaded black. Note, there is some minor distortion between the two images due to the tilt correction from the EBSD mapping. High angle grain boundaries are defined with a threshold of  $\geq 10^\circ$  of misorientation. The star symbol represents an amphibole grain with no microboudinage but shows a gradual change in misorientation. The blue, purple, and red arrows show examples of microboudinage in amphibole and their corresponding misorientation. The shear plane is parallel to the horizontal plane of each photomicrograph with a dextral shear sense. Na-Amp—sodic amphibole, Na-Ca-Amp—sodic-calcic amphibole, Ab—albite, Ep—epidote, Ilm—ilmenite, Ttn—titanite.

### 3.3. Metamorphic Reaction

The metamorphic reaction within the samples involves sodic amphibole and titanite and produces sodic-calcic amphibole, albite, and ilmenite (Equation 1).



As noted in Sections 3.2.1 and 3.2.2, the reaction occurs in both the hydrostatic and deformed samples. Microstructurally, quartz, white mica, and calcite show no reaction textures, therefore they are assumed to not be involved in the reaction (Figures 4 and 7). Ilmenite is always found at the rim of a titanite grain until the titanite has been consumed and a cluster of small ( $\sim 1\text{--}2\ \mu\text{m}$ ) ilmenite grains remain (Figures 4b and 6). Albite crystallizes as small grains, ranging from the submicron-scale to several microns, in both the hydrostatic and deformed samples in a mixed/intergrowth texture with the sodic amphibole (Figures 4, 6, and 8). In the 24-hr 700°C hydrostatic sample, albite crystallization is not homogeneous; some areas show notable amounts of albite crystallization while other areas show almost no albite crystallization even though the amphibole abundance is the same (Figure 4b). In the deformed samples, albite crystallization is more homogeneous and largely crystallizes in or near microboudin necks (Figure 8a), but there are cases where albite crystallizes within sodic amphibole grains unrelated to the process of microboudinage or the development of fractures (Figure 6a). The difference in albite crystallization between the 24-hr hydrostatic experiment and the deformed samples is the progress of the reaction. Based on the 12-hr 700°C hydrostatic experiment, we assume that the starting powder has  $\sim 2\%$  albite prior to the onset of the reaction (Figure 4d). If the 48-hr 750°C hydrostatic experiment represents a sample where the reaction is near complete, then there is an  $\sim 15\%$  increase in the modal abundance in albite as a result



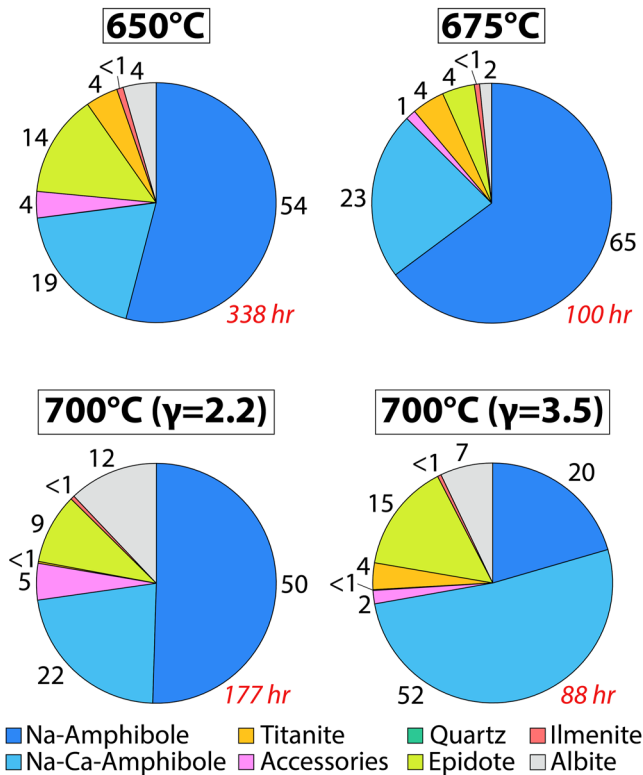


**Figure 9.** Diagrams showing the estimated modal abundance from four deformed samples based on SEM-BSE photomicrographs, where each photomicrograph is  $\sim 250 \times 250 \mu\text{m}$  in size. Due to their low abundance white micas and calcite are listed as Accessory phases. Italicized red numbers refer to the total time the samples were at peak pressure and temperature conditions (see Table 1).

of the reaction (Figure 4d). For the deformed samples conducted at 650 and 675°C, the modal abundance of albite ranges between 2% and 4% while at 700°C the modal abundance increases to 7%–12% (Figure 9). While there is an overall increase in albite within our deformed samples, there is a notable amount of titanite and sodic amphibole remaining suggesting the reaction is not complete prior to quenching. While the volume percent of albite increases within our samples over the duration of the experiments, we do not think this affects our mechanical results or interpretations because the albite does not create any significant interconnected weak layers within the samples (Figures 6 and 7). Amphibole phase diagrams show the chemical variation between the starting material (CMW blueschist), the hydrostatic sample, and the original sodic amphibole and the new sodic-calcic amphibole from the deformed samples (Figure 10). Microprobe data used to create these plots are listed in Supporting Information S1.

#### 4. Flow Law for Microboudinage

Based on the similar stress exponent values from the strain rate stepping experiments,  $n \approx 2.0$ , and the amphibole microboudinage microstructures we interpret these samples as deforming by diffusion creep rate-limited by diffusion into the microboudin necks during microboudinage. The processes of microboudinage and diffusion act in parallel, where no void space is created. Therefore, as a microboudin neck widens, new material is simultaneously diffused into the microboudin neck, making this a diffusion-controlled mechanism. A theoretical framework for microboudinage as a deformation mechanism was derived by Lehner and Bataille (1984), which we utilize to create a flow law representative of our experimental samples. For a material that deforms by microboudinage, Lehner and Bataille (1984) determined that the diffusion-controlled rate of mass transfer,  $\dot{m}_D$ , equals,

$$\dot{m}_D = \frac{\rho^f \bar{V}_o^s c_p D \sigma^n}{2ERT\delta}. \quad (2)$$

Lehner and Bataille (1984) also show that the stress exponent in Equation 2 is  $n = 2.0$  when  $\sigma_1 \neq \sigma_2 = \sigma_3$  (see Equations 60 and 61 in Lehner & Bataille, 1984), which is very similar to the stress exponents determined by our strain rate stepping experiments (Figure 2). The displacement rate can be calculated by dividing Equation 2 by the density of the solid phase,  $\rho^s$ ,

$$\frac{dx}{dt} = \frac{\rho^f \bar{V}_o^s c_p D \sigma^n}{\rho^s 2ERT\delta}, \quad (3)$$

which can then be converted into a strain rate,  $\dot{\epsilon}$ , by dividing Equation 3 by the thickness (th) of the deforming zone (e.g., the experimental shear zone thickness) yielding,

$$\dot{\epsilon} = \frac{\rho^f \bar{V}_o^s c_p D \sigma^n}{\rho^s 2ERT\delta} \frac{1}{\text{th}}. \quad (4)$$

Equation 4 can be simplified by expanding the diffusivity term (e.g.,  $D = D_o \exp\left(\frac{-Q}{RT}\right)$ ) and by condensing a number of parameters into A, ( $A = \frac{\rho^f \bar{V}_o^s c_p D_o}{\rho^s 2ERT}$ ). This results in a simplified flow law, Equation 5, consistent with previous diffusion creep flow laws (Hirth & Kohlstedt, 2003; Rutter & Brodie, 2004). However, in Equation 5,  $\delta$  is used instead of  $d$  to signify the diffusional length scale as the microboudin neck length instead of grain size. See Table 2 for definition of all symbols and their values.

$$\dot{\epsilon} = A \frac{\sigma^n}{\delta} e^{\left(\frac{-Q}{RT}\right)} \quad (5)$$

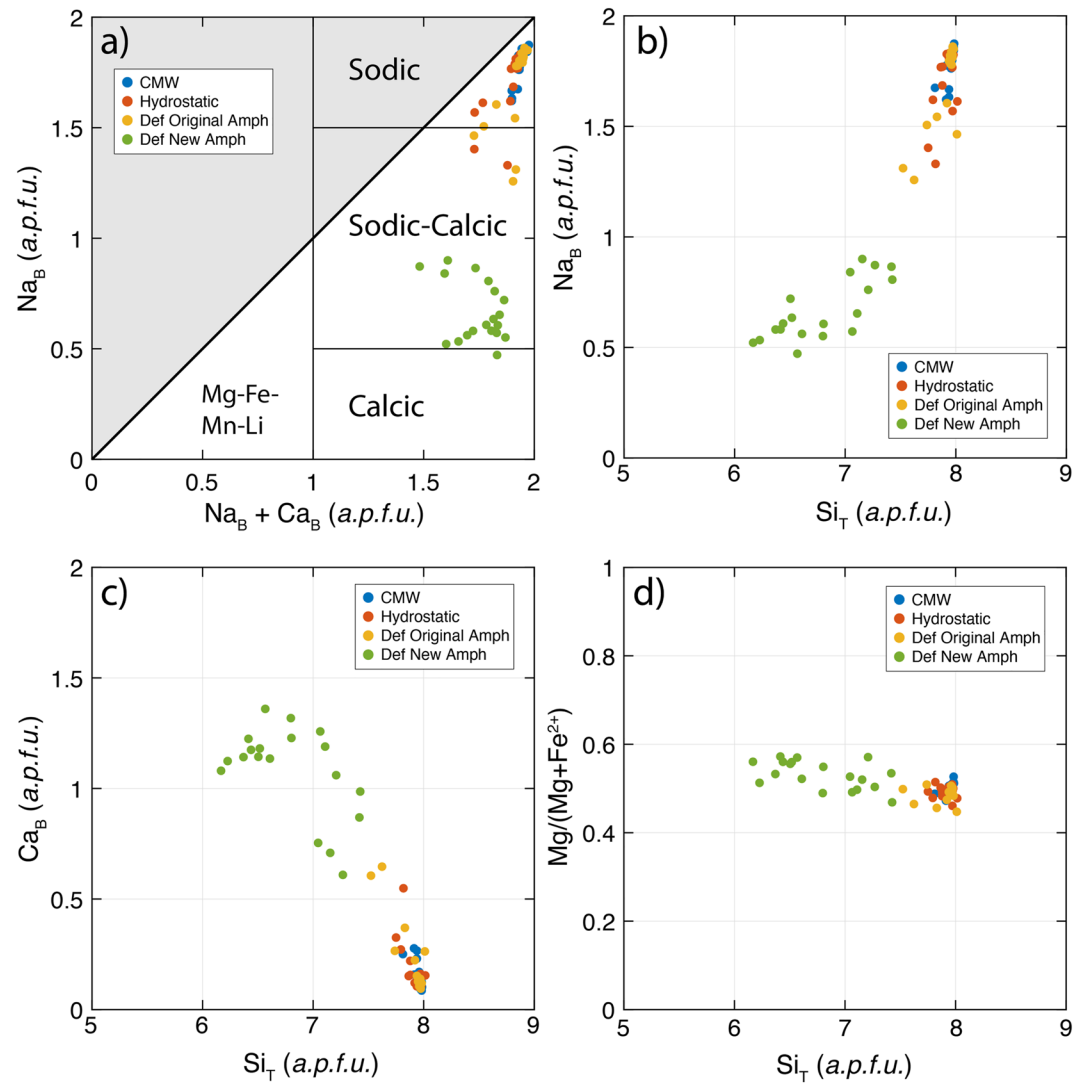


**Figure 10.** Phase diagrams overlaid with electron microprobe point analyses showing the compositional variations of amphibole used in this study. In the legend, CMW refers to the original Condrey Mountain Window sodic amphibole that was not brought to experimental temperature and pressures. *Hydrostatic* refers to the sodic amphibole within the two 700°C hydrostatic experiments, while *Def Original Amph* and *Def New Amph* refers to the original sodic amphibole and the new sodic-calcic amphibole, respectively within deformed samples LT036 (700°C) and LT044 (650°C). *a.p.f.u.* is defined as the atoms per formula unit. Data for these plots are found in Tables S1 and S2. Electron microprobe point analyses on titanite, epidote, and albite are found in Table S3.

For microboudinage, the diffusion length scale is defined as the microboudin neck length (see Figure 3 in Lehner & Bataille, 1984). For each deformation experiment at least 150 microboudin neck lengths were measured in each sample using SEM-BSE photomicrographs (Figure 11a). Based on the resolution of the BSE photomicrographs, we assume the smallest measurable microboudin neck length is 0.5  $\mu\text{m}$ . Figure 11 shows examples of measured microboudin neck lengths and the microboudin neck length histograms for the deformation experiments, respectively. We assume the average microboudin neck length is constant for all deformation steps for a given strain rate stepping experiment, which is supported by the similar mechanical data and average microboudin neck length for the constant and strain rate stepping experiments conducted at 675°C (Figures 2b and 11). The average microboudin neck lengths are listed in Table 1. Based on the similarities of our deformation microstructures and the stress exponent values to the theoretical analysis by Lehner and Bataille (1984), we assume the diffusion length scale exponent equals 1.0. Using the mechanical data and average microboudin neck length measurements, we determine the remaining flow law parameters using a robust fit least squares regression,

**Table 2**

List of Symbols and Descriptions

$\sigma$	Differential stress (MPa)
$\rho^f$	Density of the fluid (kg/m <sup>3</sup> )
$\rho^s$	Density of the solid phase (kg/m <sup>3</sup> )
$\bar{V}_o^s$	Molar volume of the reference state in the solid phase (m <sup>3</sup> /mol)
Cp	Solute concentration
D	Diffusivity (m <sup>2</sup> /s)
D <sub>o</sub>	Diffusivity at reference state (m <sup>2</sup> /s)
n	Stress exponent
E	Young's modulus (MPa)
R	Gas constant (8.314 J/K <sup>-1</sup> /mol <sup>-1</sup> )
T	Temperature (K)
$\delta$	Average boudin length ( $\mu$ m)
$\dot{\epsilon}$	Strain rate (s <sup>-1</sup> )
Q	Activation enthalpy (kJ/mol)
A	Material parameter for creep (MPa <sup>-n</sup> $\mu$ m s <sup>-1</sup> )
dx/dt	Displacement rate (m/s)
$\dot{m}_D$	Diffusion controlled rate of mass transfer (kg/m <sup>2</sup> /s)

where  $A = 2.43e11 \text{ MPa}^{-n} \mu\text{m s}^{-1}$ ,  $n = 2.0 \pm 0.3$ , and  $Q = 384 \pm 15 \text{ kJ/mol}$  with uncertainties representing one standard deviation. Figure 2b shows there is a good fit between the experimental data and the flow law. Figure S4 in Supporting Information S1 compares flow laws with different flow law parameters based on the uncertainties determined by the least squares regression (see Table S4 for different flow law parameters).

## 5. Discussion

We have shown that our experimentally deformed blueschist samples deformed primarily by microboudinage in amphibole. Below we discuss comparisons between our experimentally deformed samples and naturally deformed blueschists, the role of microboudinage as a deformation mechanism as well as the extrapolation of our flow law to geologic conditions and its implications for subduction zone rheology.

### 5.1. Comparison to Natural Blueschist and Amphibole Microstructures

Microboudinage has been well described in naturally deformed rocks as early as the late 1960s and 1970s (Draper, 1978; Misch, 1969, 1970). Amphiboles are one of the most common minerals that deform by microboudinage (Draper, 1978; Masuda et al., 2011; Misch, 1969, 1970; Schroeder & John, 2004), while this process has also been reported in pyroxene (Draper, 1978; Misch, 1970), feldspar (Gates & Glover, 1989; Grasemann et al., 1999; Ji & Li, 2021), epidote (Misch, 1969), tourmaline (Li et al., 2020; Mulch et al., 2006), biotite (Little et al., 2002) and rutile needles (Mitra, 1976; Nachlas et al., 2018). Sodic amphibole also deforms by rigid body rotation in our samples, as emphasized by the strong foliation developed at shear strains as low as  $\sim 1.5$  (Figure 6). Rigid body rotation has also been interpreted to occur in naturally (Aspiroz et al., 2007; Berger & Stunitz, 1996; Elyaszaheh et al., 2018; Tatham et al., 2008) and experimentally (Kim & Jung, 2019; Park et al., 2020) deformed amphiboles. Sodic-calcic amphibole deforms by diffusion creep and is the strain accommodating phase along with albite within the C'-shear bands (Figure 7). Albite is commonly found in pressure shadows of large epidote and quartz grains as well as C'-shear bands and is interpreted to deform by a diffusion

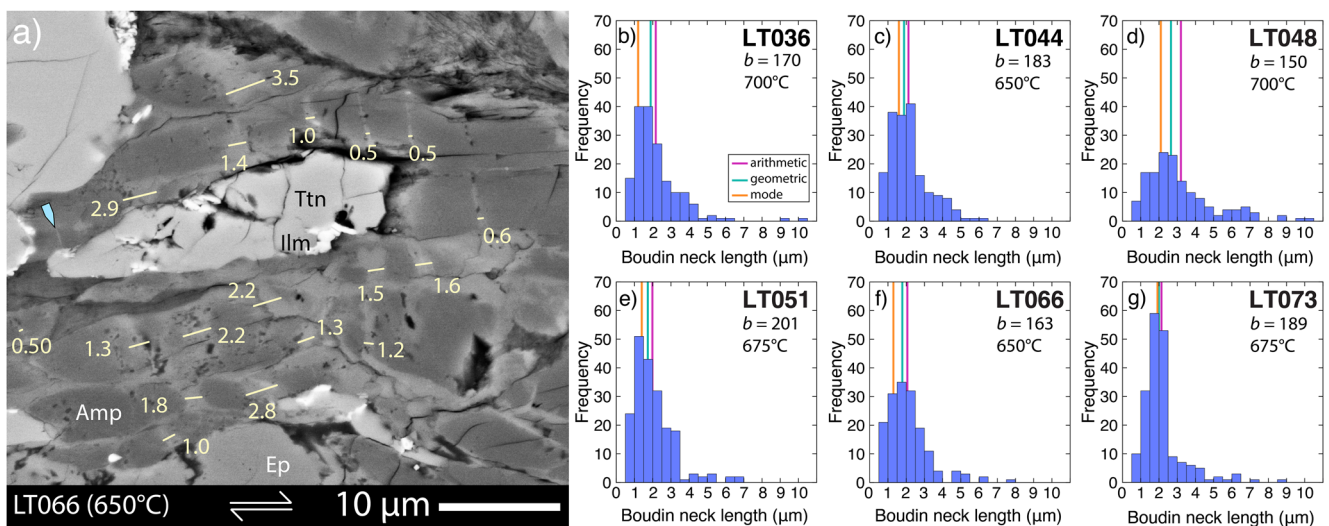


**Figure 11.** (a) BSE photomicrograph showing examples of microboudin neck length measurements used to calculate the average microboudin neck length spacing. (b–g) Histograms of microboudin neck length measurements for each deformation experiment with the arithmetic mean, geometric mean, and mode represented by the vertical lines.  $b$  refers to the number of microboudins measured in each sample. Blue arrow in (a) shows a microboudin with a distance less than  $0.5 \mu\text{m}$  that is not measured.

creep mechanism. Diffusion creep in albite has been observed in rocks from paleosubduction zones in Japan and the Central Alps (Condit et al., 2022; Ujiie et al., 2022). While there are a few amphibole grains that show evidence of internal strain through grain misorientation unrelated to microboudinage, this is rare (Figure 8). Additionally, based on the BSE-SEM photomicrograph and the corresponding GROD map, the small grains with low internal misorientation are interpreted to be the result of microboudinage and brittle fracturing of the sodic amphibole and not related to dynamic recrystallization (Figure 8). Dislocation-related deformation mechanisms are interpreted to not contribute to amphibole deformation or deformation in any other mineral within our samples. Epidote in naturally deformed blueschists typically behaves as either rigid rotating grains or by fracturing and cataclasis (Kotowski & Behr, 2019; Misch, 1969), consistent with our deformed samples. As a result of titanite breakdown, fine-grained ilmenite is interpreted to deform by a diffusion-based mechanism due to the fine grain size and lack of internal deformation features. In natural metabasic blueschists ilmenite is typically a minor component and does not significantly influence the mechanical properties (Gao et al., 1999), consistent with our deformed samples. The one notable difference between our experimental samples and naturally deformed mafic blueschists is quartz deformation. In naturally deformed blueschists, quartz typically does not deform by rigid body rotation but rather by dislocation and/or diffusion creep mechanisms (Kotowski & Behr, 2019; Misch, 1969; Omrani et al., 2013). However, for the deformation conditions of our experiments, the equivalent stress required for quartz to deform by dislocation creep is approximately 1 GPa, significantly higher than the bulk strength of our samples (Richter et al., 2018; Tokle et al., 2019). Similar to ilmenite, quartz makes up a small percentage of our samples (Figures 4d and 9), therefore likely has little effect on the mechanical data.

The albite-amphibole intergrowth textures and the change from sodic to sodic-calcic amphibole compositions are commonly observed in natural and experimental amphibole-bearing samples. High pressure deformation experiments conducted at 730°C at 2 GPa for 9 hr on a natural blueschist with 55 vol. % glaucophane shows partially reacted amphibole grains where an intergrowth texture develops within glaucophane (see Figure 3b in Bang et al., 2021). Similar to our experiments, the intergrowth texture occurs along both linear crystallographically controlled microfractures as well as throughout amphibole grain interiors. The intergrowth textures have also been observed in natural amphibole-bearing samples (Holland & Ray, 1985; Jamison, 1990; Kryza et al., 1990). The change in amphibole composition from sodic to sodic-calcic amphibole is observed in many natural amphibole-bearing samples and interpreted to represent the early or initial stages of exhumation with the transition from blueschist to greenschist facies (Gao et al., 1999; Jacobson & Sorensen, 1986; Kotowski et al., 2022; Kryza et al., 1990; Laurent et al., 2017; Omrani et al., 2013; Ring et al., 2020; Trotet et al., 2001). Wakabayashi (1990) also showed amphibole microboudinage where sodic amphibole diffuses into the boudin neck of an initially calcic amphibole, which is used as evidence to suggest a counterclockwise P-T-t path in the Franciscan Complex. Overall, the microstructures from our experimental results agree well with microstructures from previous experimental studies and many naturally deformed amphibole-bearing rocks.

## 5.2. Microboudinage as a Deformation Mechanism

Many tabular minerals in deformed rocks show microboudinage, so it is important to consider whether the process of microboudinage is rheologically controlling. In the case where microboudinage is rheologically controlling, the mineral phase exhibiting microboudinage needs to represent the load bearing phase (e.g., Handy, 1990, 1994), as in the case of our deformation experiments. Preserved examples of naturally deformed amphiboles exhibiting microboudinage as the rheologically controlling deformation mechanism, at the scale of meter-sized mafic lenses or larger, can be found in many paleosubduction zone environments, from the Northern Cascades in Washington, USA (Misch, 1969), the Blue Mountain massif in Jamaica (Draper, 1978), the Klamath mountains, USA (Tewksbury-Christle, Ph.D. thesis Chapter 4, 2021), the Zagros Orogen, southeastern Iran (Muñoz-Montecinos, Angiboust, & Garcia-Casco, 2021; Muñoz-Montecinos, Angiboust, Garcia-Casco, Glodny, & Bebout, 2021), Syros, Greece (Kotowski & Behr, 2019), the northern Appalachians, USA (Honsberger, 2023), and the Franciscan Complex, USA (Wakabayashi, 1990), with several photomicrographs shown in Figure 12. While microboudinage is commonly identified in amphibole-bearing rocks, it is not typically discussed as a rheologically significant deformation mechanism. One reason may be that amphiboles are a crystallographically continuous mineral, where new amphibole found in the boudin neck tends to grow continuously with the boudinaged grains (as shown in Figures 7 and 12); therefore, the amount of amphibole microstructures exhibiting microboudinage may be overlooked under the optical microscope. This issue was first highlighted by Misch (1969), who found examples of microboudinage in actinolite where the solid and diffusing phases were chemically very similar



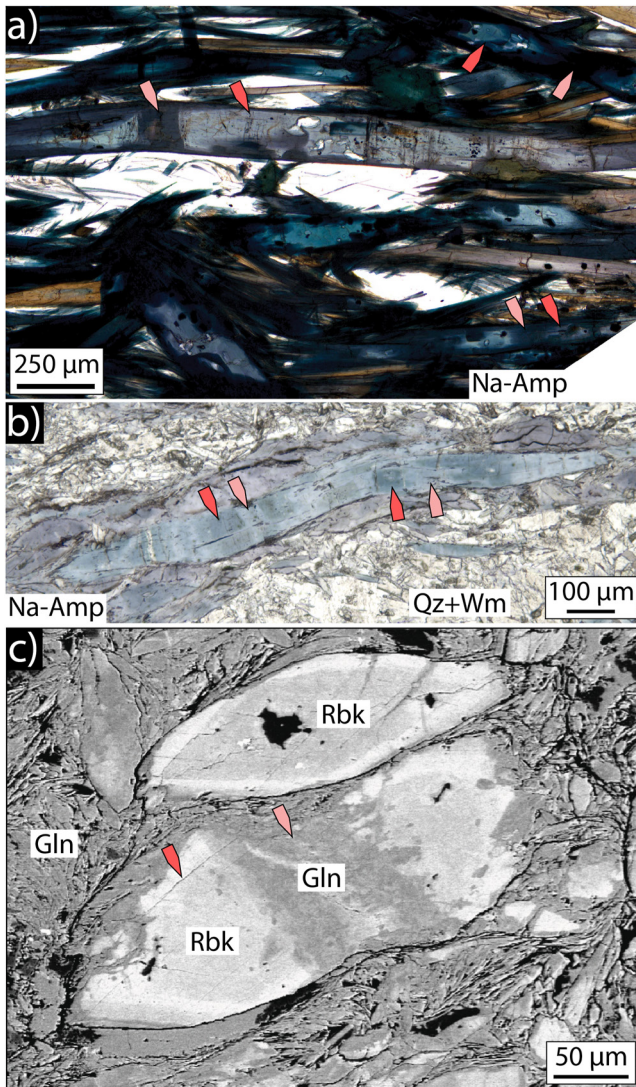


**Figure 12.** Photomicrographs showing examples of microboudinage in sodic amphiboles from (a) Klamath mountains, USA (Tewksbury-Christle, 2021 Ph.D. thesis) and (b, c) Zagros Orogen, southeastern Iran (Muñoz-Montecinos, Angiboust, Garcia-Casco, Glodny, & Bebout, 2021). Photomicrographs (a, b) are taken in plane polarized light where the blue to purple-colored minerals are amphibole and the white colored regions are quartz and/or white mica. Panel (c) is a photomicrograph taken using SEM-BSE where the two large amphibole grains are surrounded by a finer-grained matrix of amphibole. In all photomicrographs, the dark red arrows highlight the original amphibole and the light red arrows highlight the compositionally new amphibole. Na-Amp—sodic amphibole, Gln—glaucofan, Rbk—riebeckite, Qz—quartz, and Wm—white mica.

and were optically indistinguishable until the amphibole chemical variations were measured.

A key component to microboudinage as a deformation mechanism is the process of diffusion into the boudin neck. For microboudinage, if the opening rate of the boudin neck exceeds the rate of diffusion for a particular phase then other phases may also diffuse into the boudin neck (Misch, 1969). This is observed in our deformation experiments where albite is found mixed with sodic-calcic amphibole in some places, (blue arrows in Figure 8a) and unmixed in other places where albite clearly post-dates earlier sodic-calcic amphibole diffusion (blue arrows in Figure 6a). The observation of multiple phases within the boudin neck is consistent with natural examples of microboudinage in amphiboles (see Figure 5 in Misch, 1969). Given that the process of microboudinage is rate limited by diffusion into the boudin neck, the diffusing phase, the number of different phases, and the abundance of each of the diffusing phases will influence the value of the activation enthalpy,  $Q$ , which is determined to be  $384 \pm 15$  kJ/mol for our samples. Getsinger (2015, Ph.D. thesis chapter 4) determined an activation enthalpy in the range of 305–353 kJ/mol for diffusion creep in a fine-grained amphibolite containing ~40%–65% amphibole, ~20%–40% plagioclase, ~10%–20% clinopyroxene, and trace amounts of olivine, orthopyroxene, chlorite, and mica, which is consistent, albeit slightly lower than our activation enthalpy. Offerhaus et al. (2001) determined an activation enthalpy of 193 kJ/mol for diffusion creep in wet albite (see Table 1 in Rybacki & Dresen, 2004 for flow law parameters). Given the majority of the microboudin necks are dominated by sodic-calcic amphibole, the similar activation enthalpy values between our sodic-calcic amphibole and the mafic amphibole measured by Getsinger (2015), and the notable difference between our measured activation enthalpy and the activation enthalpy for wet diffusion creep in albite, we postulate that sodic-calcic amphibole is the rheologically controlling diffusional phase, although the presence of albite may influence our activation enthalpy value.

For an aggregate deforming by microboudinage, new boudins continuously develop with increasing strain but at a given amount of strain the mineral deforming by microboudinage will no longer be able to produce new microboudins. We propose that the amount of strain that can be accommodated via microboudinage scales with the aspect ratio of the original grain. Therefore, minerals like feldspar which are typically low aspect ratio grains can develop fewer microboudins (Ji & Li, 2021) than minerals such as amphibole and biotite, which can accommodate significantly more strain via microboudinage (Figure 12; Figure 8c in Little et al., 2002). This relationship may also hold for monomineralic aggregates with grains of different aspect ratios. Figure 6 shows amphibole grains with higher aspect ratios typically have more microboudins than the lower aspect ratio grains. Our highest strain sample accumulated a shear strain of 3.47 and was still deforming by microboudinage when quenched. Biotite microboudins in a mylonitic gneiss from the Alpine Fault in New Zealand were estimated to accom-

modate foliation-orthogonal shortening of ~51% (Little et al., 2002). When an aggregate is no longer able to deform by microboudinage then the aggregate will most likely deform by another mechanism defined by the rheology of the material that makes up the microboudin neck. We posit that this occurs when the microboudin neck material develops interconnected weak layers at the sample-scale or larger.  $C'$ -shear bands are examples in our blueschist samples where the rheologically weaker sodic-calcic amphibole and albite become interconnected developing local high strain regions (Figure 7). Once these regions of weak material become interconnected at the sample-scale this may change the diffusional length scale for diffusion creep in our samples.

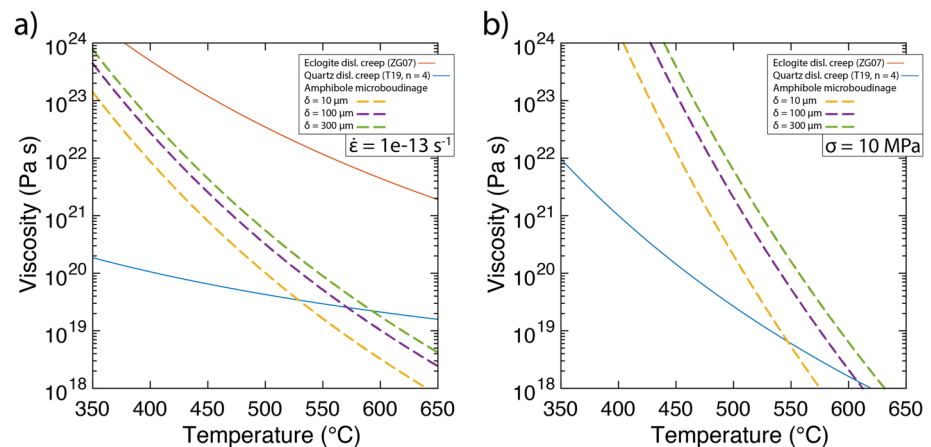


**Figure 13.** Plots of temperature versus log viscosity comparing our amphibole microboudinage flow law with the quartz dislocation creep and eclogite dislocation creep flow laws extrapolated to epidote blueschist and eclogite facies conditions where (a) viscosity is calculated assuming a constant strain rate of  $10^{-13} \text{ s}^{-1}$  and (b) viscosity is calculated assuming a constant stress of 10 MPa. Figures S5 and S6 in Supporting Information S1 show additional temperature versus viscosity plots for a range of strain rate and stress conditions. For the quartz and eclogite dislocation creep flow laws pressure varies linearly from 1.0 GPa at 350°C to 2.0 GPa 650°C, where water fugacity is calculated using Equation 2 in Shinevar et al., 2015. ZG07—Zhang and Green (2007) and T19,  $n = 4$ —Tokle et al. (2019) extrapolated flow law where  $A$  has been modified following Tokle and Hirth (2021).

Another type of microboudinage observed in amphiboles occurs where amphibole grains are isolated in a weaker matrix and a different mineral phase fills the microboudin neck, which are commonly quartz and/or calcite (Ji & Li, 2021; Li & Ji, 2020; Masuda et al., 1990, 2011; Wassman & Stöckhert, 2012). This type of microboudinage is also observed in minerals such as feldspar (Figure 6d in Gates & Glover, 1989), pyroxene (Misch, 1970; Wassman & Stöckhert, 2012), epidote (Misch, 1969), and tourmaline (Li et al., 2020; Mulch et al., 2006). These are cases where microboudinage is not the rheology controlling mechanism.

The orientation of microboudins, as well as outcrop-scale boudins, are often used as structural features to estimate the stress and strain fields of an outcrop (Goscombe et al., 2004; Masuda et al., 2011). Our deformation microstructures show largely symmetric microboudins at the grain scale (Figures 6 and 8), suggesting a predominantly co-axial deformation environment based on the classifications from Goscombe et al. (2004); however, these experiments were all conducted in the general shear geometry. The foliation of our samples, which define the orientation of the microboudins, range from  $\sim 25^\circ$  antithetic to the shear plane to parallel to the shear plane, implying that the opening orientation of the microboudins is oblique to the  $\sigma_1$  orientation of the experiments, again inconsistent with classification of boudinage from Goscombe et al. (2004). A possible explanation for this is that general shear experiments conducted in the Griggs apparatus contain a significant amount of shortening, from  $\sim 20\%$  shortening at shear strains of  $\sim 2$  up to  $30\%$ – $50\%$  shortening in experiments conducted to shear strains  $>3.5$  (Heilbronner & Tullis, 2006; Tokle, Hirth, & Stunitz, 2023). This shortening component may be sufficient in developing microboudins at oblique orientations to the  $\sigma_1$  orientation. While the geometry of microboudinage at the grain-scale shows symmetric boudinage, the  $C'$ -shear bands clearly show that deformation is dominated by shear at the sample-scale (Figure 7). This example of scale dependent observations at the grain-to sample-scales could have important implications for interpreting deformation in naturally deformed samples exhibiting microboudinage.

### 5.3. Extrapolation of the Microboudinage Flow Law and Implications for Subduction Zone Rheology

To estimate how our amphibole microboudinage flow law affects the viscosity of the subduction zone interface, we compared it with quartz and eclogite dislocation creep flow laws that represent metasediment and metamafic rheologies, respectively. We plotted these flow laws at a constant strain rate of  $1e-13 \text{ s}^{-1}$  and a constant stress of 10 MPa across a temperature range of 350–650°C (Figure 13). Based on examples of microboudinage in sodic-rich amphiboles from paleosubduction zone environments (Figure 12), we plotted three curves for the microboudinage flow law with boudin neck lengths of 10, 100, and 300  $\mu\text{m}$  (Figure 13). For quartz dislocation



creep, we used the Tokle et al. (2019) extrapolated  $n = 4$  flow law, where  $A = 8.3e-13$  following Tokle and Hirth (2021), and for eclogite dislocation creep, we used Zhang and Green (2007). Our results show that the microboudinage flow law has an intermediate viscosity between quartz and eclogite dislocation creep at temperatures below  $\sim 525$ – $550^\circ\text{C}$ , whereas the microboudinage viscosity is roughly isoviscous with quartz dislocation creep at higher temperatures,  $\sim 525$ – $600^\circ\text{C}$  (Figure 13). These estimates are consistent with field observations from paleosubduction zone environments (Kotowski & Behr, 2019; Wassman & Stöckhert, 2012). However, we acknowledge that quartz and eclogite dislocation creep are simplifying assumptions for defining the rheology of metasedimentary and metamafic rocks along the subduction zone interface. Other deformation mechanisms, such as pressure solution creep (e.g., Gratier et al., 2013; Wassman & Stöckhert, 2013) and transformational weakening (e.g., Stunitz et al., 2020), likely play a significant role in defining the rheology of the subduction zone interface, but there are no accurate flow laws to represent these mechanisms currently.

Amphibole rheology is a critical component to our understanding of intermediate to deep subduction zone dynamics. Our amphibole microboudinage flow law provides constraints on an important diffusion-controlled deformation mechanism in amphibole-bearing rocks as well as provides a quantitative method for constraining the rheology of load-bearing tabular minerals, based on the theoretical model developed by Lehner and Bataille (1984). Additionally, our flow law is unique in comparison to most laboratory derived flow laws in that we constrained a deformation mechanism that operates simultaneously with a metamorphic reaction, although this is not a requirement to activate this deformation mechanism as long as there is a chemical potential gradient driving the diffusion of material into the microboudin neck. Many tectonic environments show changes in the rheological properties of rocks occur with changes in the rocks' metamorphic state (Brodie & Rutter, 1985, 1987; Condit & Mahan, 2018; Getsinger et al., 2013; Giuntoli et al., 2018; Lee et al., 2022; Rutter & Brodie, 1985, 1995; White & Knipe, 1978); while a number experimental studies have investigated the effect of metamorphic reactions on the viscous flow of geologic materials (De Ronde et al., 2004, 2005; Getsinger & Hirth, 2014; Incel et al., 2017; Mansard et al., 2020; Marti et al., 2018; Stunitz & Tullis, 2001). The reaction of sodic- to sodic-calcic amphibole that occurs coeval with deformation in our experiments is also commonly observed in natural amphibole-bearing rocks that are transitioning from blueschist to high pressure greenschist facies, for example, during the early stages of exhumation within a subduction channel configuration (Gao et al., 1999; Jacobson & Sorensen, 1986; Kotowski et al., 2022; Kryza et al., 1990; Laurent et al., 2017; Omrani et al., 2013; Ring et al., 2020; Trotet et al., 2001). Given the extrapolation of the microboudinage flow law to subduction zone interface conditions (Figure 13), it best applies to “warm” subduction zone geotherms that lack lawsonite such as modern-day subduction in Mexico, Chile, southwest Japan and North Cascadia. The flow law also applies to exhumation in continental subduction zones where temperatures are estimated to be  $\geq 500^\circ\text{C}$  at high pressures where sodic and/or sodic-calcic amphiboles are stable (Augier et al., 2005; De Jong, 2003) or subduction zones that experience heating during exhumation such as in the western European Alps (Angiboust et al., 2019; Ernst, 1973) or the Tauern Window in the eastern European Alps (Bakker et al., 1989; Zimmermann et al., 1994). The microboudinage flow law also suggests that the influence of sediments on the viscosity of the subduction zone interface may decrease with increasing temperature, due to the decreasing viscosity contrast between amphibole microboudinage and quartz dislocation creep (Figure 13), or until the onset of eclogitization. Finally, microboudinage has been well documented in amphiboles over a wide range of chemical compositions and metamorphic conditions (Draper, 1978; Misch, 1969; Muñoz-Montecinos, Angiboust, Garcia-Casco, Glodny, & Bebout, 2021; Schroeder & John, 2004; Wakabayashi, 1990); however, given the wide range of amphibole compositions (e.g., Hawthorne et al., 2012; Leake et al., 1997), it is unclear how significant chemical variations in amphibole are in affecting the diffusional properties of amphibole. Therefore, until there is a better understanding of the effect of chemistry on amphibole rheology, we propose that the flow law developed in this study can be applied for compositionally similar amphiboles deforming via microboudinage.

## 6. Conclusions

We conducted strain rate stepping experiments in the general shear geometry on powdered natural blueschist aggregates in the Griggs apparatus at  $\sim 1.0$  GPa and temperatures ranging from  $650$  to  $700^\circ\text{C}$ . The mechanical data from the strain rate stepping experiments show stress exponents ranging from 1.8 to 2.2. Microstructural analysis shows the rheologically controlling deformation mechanism is microboudinage of sodic amphibole and diffusion of sodic-calcic amphibole into the microboudin neck. We interpreted the samples as deforming by diffusion creep of the sodic-calcic amphibole, which was rate-limited by diffusion into the boudin neck. We developed a

diffusion creep flow law with parameters of  $A = 2.43e11 \text{ MPa}^{-n} \mu\text{m s}^{-1}$ ,  $n = 2.0 \pm 0.3$ ,  $m = 1.0$ ,  $Q = 384 \pm 15 \text{ kJ/mol}$  using a least square regression. This flow law provides some of the first rheological constraints on diffusional processes in amphibole and provides a method for quantifying the rheology of tabular minerals. Extrapolation of the flow law gives intermediate viscosity estimates relative to quartz and eclogite dislocation creep consistent with field relationships from paleosubduction zone environments.

## Data Availability Statement

Data used in this study are available at Tokle, Hufford, et al. (2023), <https://doi.org/10.3929/ethz-b-000606009>.

## Acknowledgments

This research was funded by an ERC Starting Grant to W.M. Behr (S-SIM, Grant No. 947659). Thanks to Carolyn Tewkbury-Christle for letting us use her sample as starting material. Thanks to Jesus Muñoz-Montecinos for helping calculate amphibole compositions for Figure 10 as well as many fruitful discussions. Thanks to Julien Allaz for assistance on the electron microprobe, Remy Lüchinger for making the thin sections, and to Thomas Mörgeli for assistance in the Rock Physics and Mechanics Laboratory. Thanks for Cailey Condit and Keishi Okazaki for helpful reviews that improved the manuscript and editorial handling by Doug Schmidt. Open access funding provided by Eidgenössische Technische Hochschule Zurich.

## References

- Abers, G. A. (2005). Seismic low-velocity layer at the top of subducting slabs: Observations, predictions, and systematics. *Physics of the Earth and Planetary Interiors*, 149(1–2), 7–29. <https://doi.org/10.1016/j.pepi.2004.10.002>
- Agard, P., Plunder, A., Angiboust, S., Bonnet, G., & Ruh, J. (2018). The subduction plate interface: Rock record and mechanical coupling (from long to short timescales). *Lithos*, 320–321, 537–566. <https://doi.org/10.1016/j.lithos.2018.09.029>
- Angiboust, S., Agard, P., Jolivet, L., & Beyssac, O. (2019). The Zermatt-Saas ophiolite: The largest (60-km wide) and deepest (c. 70–80 km) continuous slice of oceanic lithosphere detached from a subduction zone? *Terra Nova*, 21(3), 171–180. <https://doi.org/10.1111/j.1365-3121.2009.00870.x>
- Aspiroz, M. D., Lloyd, G. E., & Fernandez, C. (2007). Development of lattice preferred orientation in clin amphiboles deformed under low-pressure metamorphic conditions. A SEM/EBSD study of metabasites from the Aracena metamorphic belt (SW Spain). *Journal of Structural Geology*, 29(4), 629–645. <https://doi.org/10.1016/j.jsg.2006.10.010>
- Audet, P., & Kim, Y. (2016). Teleseismic constraints on the geological environment of deep episodic tremor and slow earthquakes in subduction zone forearcs: A review. *Tectonophysics*, 670, 1–15. <https://doi.org/10.1016/j.tecto.2016.01.005>
- Audet, P., & Schaeffer, A. J. (2018). Fluid pressure and shear zone development over the locked to slow slip region in Cascadia. *Science Advances*, 4(3), eaar2982. <https://doi.org/10.1126/sciadv.aar2982>
- Augier, R., Agard, P., Monie, P., Jolivet, L., Robin, C., & Booth-Rea, G. (2005). Exhumation, doming and slab retreat in the Betic Cordillera (SE Spain): In situ  $^{40}\text{Ar}/^{39}\text{Ar}$  ages and P-T-d-t paths for the Nevado-Filabride complex. *Journal of Metamorphic Geology*, 23(5), 57–81. <https://doi.org/10.1111/j.1525-1314.2005.00581.x>
- Bakker, H. E., De Jong, K., Helmers, H., & Biermann, C. (1989). The geodynamic evolution of the internal zone of the Betic Cordilleras (South-East Spain): A model based on structural analysis and geothermobarometry. *Journal of Metamorphic Geology*, 7, 59–81.
- Bang, Y., Hwang, H., Kim, T., Cynn, H., Park, Y., Jung, H., et al. (2021). The stability of subducted glaucophane with the Earth's secular cooling. *Nature Communications*, 12(1), 1496. <https://doi.org/10.1038/s41467-021-21746-8>
- Bebout, G. E., & Penniston-Dorland, S. C. (2016). Fluid and mass transfer at subduction interfaces—The field metamorphic record. *Lithos*, 240–243, 228–258. <https://doi.org/10.1016/j.lithos.2015.10.007>
- Behr, W. M., & Bürgmann, R. (2021). What's down there? The structures, materials and environment of deep-seated slow slip and tremor. *Philosophical Transactions of the Royal Society A*, 379(2193), 20200218. <https://doi.org/10.1098/rsta.2020.0218>
- Behr, W. M., Holt, A., Becker, T. W., & Faccenna, C. (2022). The effects of plate interface rheology on subduction kinematics and dynamics. *Earth and Planetary Science Letters*, 479, 796–812. <https://doi.org/10.1016/j.epsl.2022.03.015>
- Berger, A., & Stunitz, H. (1996). Deformation mechanisms and reaction of hornblende: Examples from the Bergell tonalite (Central Alps). *Tectonophysics*, 257(2–4), 149–174. [https://doi.org/10.1016/0040-1951\(95\)00125-5](https://doi.org/10.1016/0040-1951(95)00125-5)
- Brodie, K. H., & Rutter, E. H. (1985). On the relationship between deformation and metamorphism with special reference to the behavior of basic rocks. In A. B. Thompson, & D. Rubie (Eds.), *Advances in physical geochemistry, Kinetics, textures and deformation* (Vol. 4). Springer Verlag.
- Brodie, K. H., & Rutter, E. H. (1987). The role of transiently fine-grained reaction products in syntectonic metamorphism: Natural and experimental examples. *Canadian Journal of Earth Sciences*, 24(3), 556–564. <https://doi.org/10.1139/e87-054>
- Condit, C. B., French, M. E., Hayles, J. A., Yeung, L. Y., Chin, E. J., & Lee, C. A. (2022). Rheology of metasedimentary rocks at the base of the subduction seismogenic zone. *Geochemistry, Geophysics, Geosystems*, 23(2), e2021GC010194. <https://doi.org/10.1029/2021GC010194>
- Condit, C. B., & Mahan, K. H. (2018). Fracturing, fluid flow and shear zone development: Relationship between chemical and mechanical properties in Proterozoic mafic dykes from southwestern Montana, USA. *Journal of Metamorphic Geology*, 36(2), 195–223. <https://doi.org/10.1111/jmg.12289>
- Conrad, C. P., Bilek, S., & Lithgow-Bertelloni, C. (2004). Great earthquakes and slab pull: Interaction between seismic coupling and plate-slab coupling. *Earth and Planetary Science Letters*, 218(1–2), 109–122. [https://doi.org/10.1016/s0012-821x\(03\)00643-5](https://doi.org/10.1016/s0012-821x(03)00643-5)
- De Jong, K. (2003). Very fast exhumation of high-pressure metamorphic rocks with excess  $^{40}\text{Ar}$  and inherited  $^{87}\text{Sr}$ , Betic Cordilleras, southern Spain. *Lithos*, 70(3–4), 91–110. [https://doi.org/10.1016/s0024-4937\(03\)00094-x](https://doi.org/10.1016/s0024-4937(03)00094-x)
- De Ronde, A. A., Heilbronner, R., Stunitz, H., & Tullis, J. (2004). Spatial correlation of deformation and mineral reaction in experimentally deformed plagioclase-olivine aggregates. *Tectonophysics*, 389(1–2), 93–109. <https://doi.org/10.1016/j.tecto.2004.07.054>
- De Ronde, A. A., Stunitz, H., Tullis, J., & Heilbronner, R. (2005). Reaction-induced weakening of plagioclase-olivine composites. *Tectonophysics*, 409(1–4), 85–106. <https://doi.org/10.1016/j.tecto.2005.08.008>
- Draper, G. (1978). Coaxial pure shear in Jamaican blueschists and deformation associated with subduction. *Nature*, 275(5682), 735–736. <https://doi.org/10.1038/275735a0>
- Elyazadeh, R., Prior, D. J., Sarkarinejad, K., & Mansouri, H. (2018). Different slip systems controlling crystallographic preferred orientation and intracrystalline deformation of amphibole in mylonites from the Neyriz mantle diapir, Iran. *Journal of Structural Geology*, 107, 38–52. <https://doi.org/10.1016/j.jsg.2017.11.020>
- Ernst, W. G. (1973). Blueschist metamorphism and PT regimes in active subduction zones. *Tectonophysics*, 17(3), 255–272. [https://doi.org/10.1016/0040-1951\(73\)90006-1](https://doi.org/10.1016/0040-1951(73)90006-1)
- Fagerang, A., & Sibson, R. H. (2010). Melange rheology and seismic style. *Geology*, 38(8), 751–754. <https://doi.org/10.1130/g30868.1>
- Gao, J., Klemd, R., Zhang, L., Wang, Z., & Xiao, X. (1999). P-T path of high-pressure/low-temperature rocks and tectonic implications in the western Tianshan Mountains, NW China. *Journal of Metamorphic Geology*, 17(6), 621–636. <https://doi.org/10.1046/j.1525-1314.1999.00219.x>
- Gates, A. E., & Glover, L. (1989). Alleghanian tectono-thermal evolution of the dextral transcurrent Hylas zone, Virginia Piedmont U.S.A. *Journal of Structural Geology*, 11(4), 407–419. [https://doi.org/10.1016/0191-8141\(89\)90018-7](https://doi.org/10.1016/0191-8141(89)90018-7)

- Getsinger, A. J. (2015). The rheology of amphibolite. Ph.D. thesis. Brown University.
- Getsinger, A. J., & Hirth, G. (2014). Amphibole fabric formation during diffusion creep and the rheology of shear zones. *Geology*, *42*(6), 535–538. <https://doi.org/10.1130/g35327.1>
- Getsinger, A. J., Hirth, G., Stünitz, H., & Goergen, E. T. (2013). Influence of water on rheology and strain localization in the lower continental crust. *Geochemistry, Geophysics, Geosystems*, *14*(7), 2247–2264. <https://doi.org/10.1002/ggge.20148>
- Giuntoli, F., Menegon, L., & Warren, C. J. (2018). Replacement reactions and deformation by dissolution and precipitation processes in amphibolites. *Journal of Metamorphic Geology*, *36*(9), 1263–1286. <https://doi.org/10.1111/jmg.12445>
- Goscombe, B. D., Passchier, C. W., & Hand, M. (2004). Boudinage classification: End-member boudin types and modified boudin structures. *Journal of Structural Geology*, *26*(4), 739–763. <https://doi.org/10.1016/j.jsg.2003.08.015>
- Grasemann, B., Fritz, H., & Vannay, J.-C. (1999). Quantitative kinematic flow analysis from the Main Central Thrust Zone (NW-Himalaya, India): Implications for a decelerating strain path and the extrusion of orogenic wedges. *Journal of Structural Geology*, *21*(7), 837–853. [https://doi.org/10.1016/s0191-8141\(99\)00077-2](https://doi.org/10.1016/s0191-8141(99)00077-2)
- Gratier, J.-P., Dysthe, D. K., & Renard, F. (2013). The role of pressure solution creep in the ductility of the earth's upper crust. *Advances in Geophysics*, *54*, 47–179. <https://doi.org/10.1016/b978-0-12-380940-7.00002-0>
- Hacker, B. R., & Christie, J. M. (1990). Brittle/ductile and plastic/cataclastic transitions in experimentally deformed and metamorphosed amphibolite. In A. G. Duba, W. B. Durham, J. W. Handin, & H. F. Wang (Eds.), *The brittle-ductile transition in rocks: American geophysical union geophysical monograph 56* (pp. 127–147). <https://doi.org/10.1029/GM056p0127>
- Handy, M. R. (1990). The solid-state flow of polymineralic rocks. *Journal of Geophysical Research*, *95*(B6), 8647–8661. <https://doi.org/10.1029/jb095ib06p08647>
- Handy, M. R. (1994). Flow laws for rocks containing two non-linear viscous phases: A phenomenological approach. *Journal of Structural Geology*, *16*(3), 287–301. [https://doi.org/10.1016/0191-8141\(94\)90035-3](https://doi.org/10.1016/0191-8141(94)90035-3)
- Hawthorne, F. C., Oberti, R., Harlow, G. E., Maresch, W. V., Martin, R. F., Schumacher, J. C., & Welch, M. D. (2012). Nomenclature of the amphibole supergroup. *American Mineralogist*, *97*(11–12), 2031–2048. <https://doi.org/10.2138/am.2012.4276>
- Heilbronner, R., & Tullis, J. (2006). Evolution of c axis pole figures and grain size during dynamic recrystallization: Results from experimentally sheared quartzite. *Journal of Geophysical Research: Solid Earth*, *111*(B10), B10202. <https://doi.org/10.1029/2005JB004194>
- Helper, M. (1986). *Deformation and high P/T metamorphism in the central part of the Condrey Mountain window, north-central Klamath Mountains, California and Oregon* (Vol. 164, pp. 125–142). GSA Memoir.
- Hielscher, R., & Schaeben, H. (2008). A novel pole figure inversion method: Specification of the MTEX algorithm. *Journal of Applied Crystallography*, *41*(6), 1024–1037. <https://doi.org/10.1107/S0021889808030112>
- Hirose, F., Nakajima, J., & Hasegawa, A. (2008). Three-dimensional seismic velocity structure and configuration of the Philippine Sea slab in southwest Japan estimated by double-difference tomography. *Journal of Geophysical Research*, *113*(B9), B09315. <https://doi.org/10.1029/2007JB005274>
- Hirth, G., & Kohlstedt, D. L. (2003). Rheology of the mantle wedge. In J. Eiler (Ed.), *Inside the subduction factory, Geophysical monograph series* (Vol. 138, pp. 83–55). AGU.
- Holland, T. J. B., & Ray, N. J. (1985). Glaucofanite and pyroxene breakdown reactions in the Pennine units of the Eastern Alps. *Journal of Metamorphic Geology*, *3*(4), 417–438. <https://doi.org/10.1111/j.1525-1314.1985.tb00328.x>
- Holyoke, C. W., & Kronenberg, A. K. (2010). Accurate differential stress measurement using the molten salt cell and solid salt assemblies in the Griggs apparatus with applications to strength, piezometers and rheology. *Tectonophysics*, *494*(1–2), 18–31. <https://doi.org/10.1016/j.tecto.2010.08.001>
- Honsberger, I. W. (2023). Newly recognized blueschist-facies metamorphism (glaucofanite-omphacite-garnet), Belvidere Mountain Complex, northern Appalachians. *Geosphere*, *19*(3), 645–653. <https://doi.org/10.1130/GES02582.1>
- Incel, S., Hilaret, N., Labrousse, L., John, T., Deldicque, D., Ferrand, T., et al. (2017). Laboratory earthquakes triggered during eclogitization of lawsonite-bearing blueschists. *Earth and Planetary Science Letters*, *459*, 320–331. <https://doi.org/10.1016/j.epsl.2016.11.047>
- Jacobson, C. E., & Sorensen, S. S. (1986). Amphibole compositions and metamorphic history of the Rand Schist and the greenschist unit of the Catalina Schist, southern California. *Contributions to Mineralogy and Petrology*, *92*(3), 308–315. <https://doi.org/10.1007/bf00572159>
- Jamison, R. A. (1990). Metamorphism of an early Palaeozoic continental margin, western Baie Verte Peninsula, Newfoundland. *Journal of Metamorphic Geology*, *8*, 269–288.
- Ji, S., & Li, L. (2021). Feldspar microboudinage paleopiezometer and its application to estimating differential stress magnitudes in the continental middle crust (examples from west Yunnan, China). *Tectonophysics*, *805*, 228778. <https://doi.org/10.1016/j.tecto.2021.228778>
- Kim, D., Katayama, I., Michibayashi, K., & Tsujimori, T. (2013). Deformation fabrics of natural blueschists and implications for seismic anisotropy in subducting oceanic crust. *Physics of the Earth and Planetary Interiors*, *222*, 8–21. <https://doi.org/10.1016/j.pepi.2013.06.011>
- Kim, D., Katayama, I., Wallis, S., Michibayashi, K., Miyake, A., Seto, Y., & Azuma, S. (2015). Deformation microstructures of glaucofanite and lawsonite in experimentally deformed blueschists: Implications for intermediate-depth intraplate earthquakes. *Journal of Geophysical Research: Solid Earth*, *120*(2), 1229–1242. <https://doi.org/10.1002/2014jb011528>
- Kim, J., & Jung, H. (2019). New crystal preferred orientation of amphibole experimentally found in simple shear. *Geophysical Research Letters*, *46*(22), 12996–13005. <https://doi.org/10.1029/2019GL085189>
- Ko, B., & Jung, H. (2015). Crystal preferred orientation of an amphibole experimentally deformed by simple shear. *Nature Communications*, *6*(1), 6586. <https://doi.org/10.1038/ncomms7586>
- Kotowski, A. J., & Behr, W. M. (2019). Length scales and types of heterogeneities along the deep subduction interface: Insights from exhumed rocks on Syros Island, Greece. *Geosphere*, *15*(4), 1038–1065. <https://doi.org/10.1130/GES02037.1>
- Kotowski, A. J., Cisneros, M., Behr, W. M., Stockli, D. F., Soukis, K., Barnes, J. D., & Ortega-Arroyo, D. (2022). Subduction, underplating, and return flow recorded in the Cycladic Blueschist Unit Exposed on Syros, Greece. *Tectonics*, *41*(6), e2020TC006528. <https://doi.org/10.1029/2020TC006528>
- Kryza, R., Muszynski, A., & Vielzeuf, D. (1990). Glaucofanite-bearing assemblage overprinted by greenschist-facies metamorphism in the Variscan Kaczawa complex, Sudetes, Poland. *Journal of Metamorphic Geology*, *8*(3), 345–355. <https://doi.org/10.1111/j.1525-1314.1990.tb00477.x>
- Laurent, V., Lanari, P., Nair, I., Augier, R., Lahfid, A., & Jolivet, L. (2017). Exhumation of eclogite and blueschist (Cyclades, Greece): Pressure-temperature evolution determined by thermobarometry and garnet equilibrium modelling. *Journal of Metamorphic Geology*, *36*(6), 769–798. <https://doi.org/10.1111/jmg.12309>
- Leake, B. E., Woolley, A. R., Arps, C. E. S., Birch, W. D., Gilbert, M. C., Grice, J. D., et al. (1997). Nomenclature of amphiboles; report of the subcommittee on amphiboles of the international mineralogical association, commission on new mineral names. *The Canadian Mineralogist*, *35*(1), 219–246.

- Lee, A. L., Stunitz, H., Soret, M., & Battisti, M. A. (2022). Dissolution precipitation creep as a process for the strain localization in mafic rocks. *Journal of Structural Geology*, *155*, 104505. <https://doi.org/10.1016/j.jsg.2021.104505>
- Lehner, F. K., & Bataille, J. (1984). Nonequilibrium thermodynamics of pressure solution. *Pure and Applied Geophysics*, *122*(1), 53–58. <https://doi.org/10.1007/bf00879649>
- Li, L., & Ji, S. (2020). On microboudin paleopiezometers and their applications to constrain stress variations in tectonites. *Journal of Structural Geology*, *130*, 103928. <https://doi.org/10.1016/j.jsg.2019.103928>
- Li, L., Ji, S., & Lin, W. (2020). Tourmaline microboudinage: An indicator of its host rheology. *Journal of Structural Geology*, *138*, 104096. <https://doi.org/10.1016/j.jsg.2020.104096>
- Little, T. A., Holcombe, R. J., & Ilg, B. R. (2002). Kinematics of oblique collision and ramping inferred from microstructures and strain in middle crustal rocks, central Southern Alps, New Zealand. *Journal of Structural Geology*, *24*(1), 219–239. [https://doi.org/10.1016/S0191-8141\(01\)00060-8](https://doi.org/10.1016/S0191-8141(01)00060-8)
- Mansard, N., Stunitz, H., Raimbourg, H., & Precigout, J. (2020). The role of deformation-reaction interactions to localize strain in polymineralic rocks: Insights from experimentally deformed plagioclase-pyroxene assemblages. *Journal of Structural Geology*, *134*, 104008. <https://doi.org/10.1016/j.jsg.2020.104008>
- Marti, S., Stunitz, H., Heilbronner, R., Plumper, O., & Kilian, R. (2018). Syn-kinematic hydration reactions, grain size reduction, and dissolution—Precipitation creep in experimentally deformed plagioclase—Pyroxene mixtures. *EGU Solid Earth*, *9*(4), 985–1009. <https://doi.org/10.5194/se-9-985-2018>
- Maruyama, S., Liou, J., & Terabayashi, M. (1996). Blueschists and eclogites of the world and their exhumation. *International Geology Review*, *38*(6), 485–594. <https://doi.org/10.1080/00206819709465347>
- Masuda, T., Miyake, T., Kimura, N., & Okamoto, A. (2011). Application of the microboudin method to palaeodifferential stress analysis of deformed impure marbles from Syros, Greece: Implications for grain-size and calcite-twin piezometers. *Journal of Structural Geology*, *33*(1), 20–31. <https://doi.org/10.1016/j.jsg.2010.11.002>
- Masuda, T., Shibutani, T., Kuriyama, M., & Igarashi, T. (1990). Development of microboudinage: An estimate of changing differential stress with increasing strain. *Tectonophysics*, *178*(2–4), 379–387. [https://doi.org/10.1016/0040-1951\(90\)90160-a](https://doi.org/10.1016/0040-1951(90)90160-a)
- Misch, P. (1969). Paracrystalline microboudinage of zoned grains and other criteria for synkinematic growth of metamorphic minerals. *American Journal of Science*, *267*(1), 43–63. <https://doi.org/10.2475/ajs.267.1.43>
- Misch, P. (1970). Paracrystalline microboudinage in a metamorphic reaction sequence. *Geological Society of America Bulletin*, *81*(8), 2483–2486. [https://doi.org/10.1130/0016-7606\(1970\)81\[2483:pmiamr\]2.0.co;2](https://doi.org/10.1130/0016-7606(1970)81[2483:pmiamr]2.0.co;2)
- Mitra, S. (1976). A quantitative study of deformation mechanisms and finite strain in quartzites. *Contributions to Mineralogy and Petrology*, *59*(2), 203–226. <https://doi.org/10.1007/bf00371309>
- Mulch, A., Teyssier, C., Cosca, M. A., & Vennemann, T. W. (2006). Thermomechanical analysis of strain localization in a ductile detachment zone. *Journal of Geophysical Research*, *111*(B12), B12405. <https://doi.org/10.1029/2005JB00432>
- Muñoz-Montecinos, J., Angiboust, S., & Garcia-Casco, A. (2021). Blueschist-facies paleo-earthquakes in a serpentinite channel (Zagros suture, Iran) enlighten seismogenesis in Mariana-type subduction margins. *Earth and Planetary Science Letters*, *573*, 117135. <https://doi.org/10.1016/j.epsl.2021.117135>
- Muñoz-Montecinos, J., Angiboust, S., Garcia-Casco, A., Glodny, J., & Bebout, G. (2021). Episodic hydrofracturing and large-scale flushing along deep subduction interfaces: Implications for fluid transfer and carbon recycling (Zagros Orogen, southeastern Iran). *Chemical Geology*, *571*, 120173. <https://doi.org/10.1016/j.chemgeo.2021.120173>
- Muñoz-Montecinos, J., Angiboust, S., Garcia-Casco, A., & Raimondo, T. (2023). Shattered veins elucidate brittle creep processes in the deep slow slip and tremor region. *Tectonics*, *42*(4), e2022TC007605. <https://doi.org/10.1029/2022TC007605>
- Nachlas, W. O., Teyssier, C., Whitney, D. L., & Hirth, G. (2018). Diffusion geospeedometry in natural and experimental shear zones. *Earth and Planetary Science Letters*, *498*, 129–139. <https://doi.org/10.1016/j.epsl.2018.06.025>
- Nyman, M. W., Law, R. D., & Smelik, E. A. (1992). Cataclastic deformation mechanism for the development of core-mantle structures in amphibole. *Geology*, *20*(5), 455–458. [https://doi.org/10.1130/0091-7613\(1992\)020<0455:cdmftd>2.3.co;2](https://doi.org/10.1130/0091-7613(1992)020<0455:cdmftd>2.3.co;2)
- Offerhaus, L. J., Wirth, R., & Dresen, G. (2001). High-temperature creep of polycrystalline albite. In S. deMeer (Ed.), et al. (Eds.), *Deformation mechanisms, rheology and tectonics* (p. 124). Utrecht University.
- Okazaki, K., & Hirth, G. (2016). Dehydration of lawsonite could trigger earthquakes in subducting oceanic crust. *Nature*, *530*(7588), 81–84. <https://doi.org/10.1038/nature16501>
- Okazaki, K., & Hirth, G. (2020). Deformation of mafic schists from subducted oceanic crust at high pressure and temperature conditions. *Tectonophysics*, *774*, 228217. <https://doi.org/10.1016/j.tecto.2019.228217>
- Omrani, H., Moazzen, M., Oberhänsli, R., Altenberger, U., & Lange, M. (2013). The Sabzevar blueschists of the North-Central Iranian micro-continent as remnants of the Neotethys-related oceanic crust subduction. *International Journal of Earth Sciences*, *102*(5), 1491–1512. <https://doi.org/10.1007/s00531-013-0881-9>
- Pacheco, J. F., Sykes, L. R., & Scholz, C. H. (1993). Nature of seismic coupling along simple plate boundaries of the subduction type. *Journal of Geophysical Research*, *98*(B8), 14133–14159. <https://doi.org/10.1029/93jb00349>
- Park, Y., & Jung, H. (2022). Seismic velocity and anisotropy of glaucophane and epidote in experimentally deformed epidote blueschist and implications for seismic properties in warm subduction zones. *Earth and Planetary Science Letters*, *598*, 117822. <https://doi.org/10.1016/j.epsl.2022.117822>
- Park, Y., Jung, S., & Jung, H. (2020). Lattice preferred orientation and deformation microstructures of glaucophane and epidote in experimentally deformed epidote blueschist at high pressure. *Minerals*, *10*(9), 803. <https://doi.org/10.3390/min10090803>
- Paterson, M. S., & Olgaard, D. L. (2000). Rock deformation tests to large shear strains in torsion. *Journal of Structural Geology*, *22*(9), 1341–1358. [https://doi.org/10.1016/S0191-8141\(00\)00042-0](https://doi.org/10.1016/S0191-8141(00)00042-0)
- Reynard, B., Gillet, P., & Willaime, C. (1989). Deformation mechanisms in naturally deformed glaucophanes: A TEM and HREM study. *European Journal of Mineralogy*, *1*(5), 611–624. <https://doi.org/10.1127/ejm/1/5/0611>
- Richter, B., Stunitz, H., & Heilbronner, R. (2018). The brittle-to-viscous transition in polycrystalline quartz: An experimental study. *Journal of Structural Geology*, *114*, 1–21. <https://doi.org/10.1016/j.jsg.2018.06.005>
- Ring, U., Pantazides, H., Glodny, J., & Skelton, A. (2020). Forced return flow deep in the subduction channel, Syros, Greece. *Tectonics*, *39*(1), e2019TC005768. <https://doi.org/10.1029/2019tc005768>
- Rutter, E. H., & Brodie, K. H. (1985). The permeation of water into hydrating shear zones. In *Metamorphic reactions: Kinetics, textures, and deformation* (pp. 242–250). Springer. [https://doi.org/10.1007/978-1-4612-5066-1\\_9](https://doi.org/10.1007/978-1-4612-5066-1_9)
- Rutter, E. H., & Brodie, K. H. (1995). Mechanistic interactions between deformation and metamorphism. *Geological Journal*, *30*(3–4), 227–240. <https://doi.org/10.1002/gj.3350300304>



- Rutter, E. H., & Brodie, K. H. (2004). Experimental grain size-sensitive flow of hot-pressed Brazilian quartz aggregates. *Journal of Structural Geology*, 26(11), 2011–2023. <https://doi.org/10.1016/j.jsg.2004.04.006>
- Rybacki, E., & Dresen, G. (2004). Deformation mechanism maps for feldspar rocks. *Tectonophysics*, 382(3–4), 173–187. <https://doi.org/10.1016/j.tecto.2004.01.006>
- Schroeder, T., & John, B. E. (2004). Strain localization on an oceanic detachment fault system, Atlantis Massif, 30°N, Mid-Atlantic Ridge. *Geochemistry, Geophysics, Geosystems*, 5(11), Q11007. <https://doi.org/10.1029/2004GC000728>
- Shinevar, W. J., Behn, M. D., & Hirth, G. (2015). Compositional dependence of crustal viscosity. *Geophysical Research Letters*, 42(20), 8333–8340. <https://doi.org/10.1002/2015gl065459>
- Skrotzki, W. (1992). Defect structure and deformation mechanisms in naturally deformed hornblende. *Physica Status Solidi A*, 131(2), 605–624. <https://doi.org/10.1002/pssa.2211310232>
- Stunitz, H., Neufeld, K., Heilbronner, R., Finstad, A. K., Konopasek, J., & Mackenzie, J. R. (2020). Transformation weakening: Diffusion creep in eclogites as a result of interaction of mineral reactions and deformation. *Journal of Structural Geology*, 139, 104129. <https://doi.org/10.1016/j.jsg.2020.104129>
- Stunitz, H., & Tullis, J. (2001). Weakening and strain localization produced by syn-deformational reaction of plagioclase. *International Journal of Earth Sciences*, 90(1), 136–148. [https://doi.org/10.1016/S0012-821X\(98\)00029-6](https://doi.org/10.1016/S0012-821X(98)00029-6)
- Tatham, D. J., Lloyd, G. E., Butler, R. W. H., & Casey, M. (2008). Amphibole and lower crustal seismic properties. *Earth and Planetary Science Letters*, 267(1–2), 118–128. <https://doi.org/10.1016/j.epsl.2007.11.042>
- Tewksbury-Christle, C. M. (2021). The rock record of subduction interface rheology, underplating processes, and seismic signatures: A case study from the Condrey Mountain Schist, northern California and southern Oregon. Ph.D. thesis.
- Tewksbury-Christle, C. M., Behr, W. M., & Helper, M. (2021). Tracking deep sediment underplating in a fossil subduction margin: Implications for interface rheology and mass and volatile recycling. *Geochemistry, Geophysics, Geosystems*, 22(3), e2020GC009463. <https://doi.org/10.1029/2020gc009463>
- Tokle, L., & Hirth, G. (2021). Assessment of quartz grain growth and the application of the wattmeter to predict quartz recrystallized grain sizes. *Journal of Geophysical Research: Solid Earth*, 126(7), e2020JB021475. <https://doi.org/10.1029/2020jb021475>
- Tokle, L., Hirth, G., & Behr, W. M. (2019). Flow law and fabric transition in wet quartzite. *Earth and Planetary Science Letters*, 505, 152–161. <https://doi.org/10.1016/j.epsl.2018.10.017>
- Tokle, L., Hirth, G., & Stunitz, H. (2023). The effect of muscovite on the microstructural evolution and rheology of quartzite in general shear. *Journal of Structural Geology*, 169, 104835. <https://doi.org/10.1016/j.jsg.2023.104835>
- Tokle, L., Hufford, L., Behr, W. M., Morales, L. F. G., & Madonna, C. (2023). Diffusion creep of sodic amphibole-bearing blueschist limited by microboudinage [Dataset]. ETH Research Collection. <https://doi.org/10.3929/ethz-b-000606009>
- Trotet, F., Vidal, O., & Jolivet, L. (2001). Exhumation of Syros and Sifnos metamorphic rocks (Cyclades, Greece). New constraints on the P-T paths. *European Journal of Mineralogy*, 13(5), 901–920. <https://doi.org/10.1127/0935-1221/2001/0013/0901>
- Tulley, C. J., Fagerang, A., & Ujiie, K. (2020). Hydrous oceanic crust hosts megathrust creep at low shear stresses. *Science Advances*, 6, eaba1529. <https://doi.org/10.1126/sciadv.aba1529>
- Ujiie, K., Noro, K., Shigematsu, N., Fagerang, A., Nishiyama, N., Tulley, C. J., et al. (2022). Megathrust shear modulated by albite metasomatism in subduction melanges. *Geochemistry, Geophysics, Geosystems*, 23(8), e2022GC010569. <https://doi.org/10.1029/2022GC010569>
- Uyeda, S., & Kanamori, H. (1979). Back-arc opening and the mode of subduction. *Journal of Geophysical Research*, 84(B3), 1049. <https://doi.org/10.1029/jb084ib03p01049>
- Wakabayashi, J. (1990). Counterclockwise P-T-t paths from amphibolites, Franciscan Complex, California: Relics from the early stages of subduction zone metamorphism. *The Journal of Geology*, 98(5), 657–680. <https://doi.org/10.1086/629432>
- Wassman, S., & Stöckhert, B. (2012). Matrix deformation mechanisms in HP-LT tectonic melanges—Microstructural record of jadeite blueschist from the Franciscan Complex, California. *Tectonophysics*, 568–569, 135–153. <https://doi.org/10.1016/j.tecto.2012.01.009>
- Wassman, S., & Stöckhert, B. (2013). Rheology of the plate interface—Dissolution precipitation creep in high pressure metamorphic rocks. *Tectonophysics*, 608, 1–29. <https://doi.org/10.1016/j.tecto.2013.09.030>
- White, S. H., & Knipe, R. J. (1978). Transformation- and reaction-enhanced ductility in rocks. *Journal of the Geological Society*, 135(5), 513–516. <https://doi.org/10.1144/gsjgs.135.5.0513>
- Yañez, G., & Cembrano, J. (2004). Role of viscous plate coupling in the late Tertiary Andean tectonics. *Journal of Geophysical Research*, 109(B2), B02407. <https://doi.org/10.1029/2003jb002494>
- Zhang, J., & Green, H. W. (2007). Experimental investigation of eclogite rheology and its fabrics at high temperature and pressure. *Journal of Metamorphic Geology*, 25(2), 97–115. <https://doi.org/10.1111/j.1525-1314.2006.00684.x>
- Zimmermann, R., Hammerschmidt, K., & Franz, G. (1994). Eocene high pressure metamorphism in the Penninic units of the Tauern Window (Eastern Alps): Evidence from <sup>40</sup>Ar-<sup>39</sup>Ar dating and petrological investigations. *Contributions to Mineralogy and Petrology*, 117(2), 175–186. <https://doi.org/10.1007/bf00286841>

## References From the Supporting Information

- Donovan, J. J., & Tingle, T. N. (1996). An improved mean atomic number background correction for quantitative microanalysis. *Microscopy and Microanalysis*, 2(1), 1–7. <https://doi.org/10.1017/S1431927696210013>